

FACULTY
OF MATHEMATICS
AND PHYSICS
Charles University

1

BACHELOR THESIS

2

Martin Vavřík

3

**Simulation and Reconstruction
of Charged Particle Trajectories
in an Atypic Time Projection Chamber**

4

5

Institute of Particle and Nuclear Physics

6

Supervisor of the bachelor thesis: Mgr. Tomáš Sýkora, Ph.D.

7

Study programme: Physics

8

Prague 2025

- ⁹ I declare that I carried out this bachelor thesis independently, and only with the
¹⁰ cited sources, literature and other professional sources. It has not been used to
¹¹ obtain another or the same degree.
- ¹² I understand that my work relates to the rights and obligations under the Act
¹³ No. 121/2000 Sb., the Copyright Act, as amended, in particular the fact that the
¹⁴ Charles University has the right to conclude a license agreement on the use of this
¹⁵ work as a school work pursuant to Section 60 subsection 1 of the Copyright Act.

In date
Author's signature

Title: Simulation and Reconstruction of Charged Particle Trajectories in an Atypical Time Projection Chamber *Added hyphen to avoid overfull hbox*

Author: Martin Vavřík

Institute: Institute of Particle and Nuclear Physics

Supervisor: Mgr. Tomáš Sýkora, Ph.D., Institute of Particle and Nuclear Physics

Abstract: Abstract.

Keywords: key words

¹⁷ Contents

¹⁸	Motivation	3
¹⁹	0.1 ATOMKI Anomaly	3
²⁰	0.1.1 ATOMKI Measurements	3
²¹	0.1.2 Other Experiments	4
²²	0.2 X17 Project at IEAP CTU	6
²³	1 Time Projection Chamber	9
²⁴	1.1 Charge transport in gases	9
²⁵	1.1.1 Drift	9
²⁶	1.1.2 Diffusion	11
²⁷	1.2 Readout	12
²⁸	1.2.1 Multi-Wire Proportional Chamber	12
²⁹	1.2.2 Gas Electron Multiplier	12
³⁰	1.2.3 Micromegas	12
³¹	1.2.4 Parallel Plate Chamber	14
³²	1.3 Orthogonal Fields TPC at IEAP CTU	14
³³	1.3.1 Motivation and Associated Challenges	14
³⁴	1.3.2 Coordinate Systems and Dimensions	14
³⁵	1.3.3 Magnetic Field Simulation	17
³⁶	2 Track Simulation	20
³⁷	2.1 Microscopic Simulation	20
³⁸	2.2 Runge-Kutta Simulation	22
³⁹	3 Track Reconstruction	24
⁴⁰	3.1 Reconstruction Assuming Steady Drift	24
⁴¹	3.2 Ionization Electron Map	26
⁴²	3.2.1 Gradient Descent Algorithm	29
⁴³	3.2.2 Interpolation on the Inverse Grid	30
⁴⁴	3.3 Discrete Reconstruction	32
⁴⁵	4 Energy Reconstruction	34
⁴⁶	4.1 Cubic Spline Fit	34
⁴⁷	4.2 Circle and Lines Fit	36
⁴⁸	4.2.1 Two-dimensional fit	37
⁴⁹	4.2.2 Three-dimensional fit	38
⁵⁰	4.3 Runge-Kutta Fit	40
⁵¹	Conclusion	45
⁵²	Bibliography	48
⁵³	List of Figures	52
⁵⁴	List of Tables	54

⁵⁶ Motivation

⁵⁷ A Time Projection Chamber (TPC) [refs] is a type of gaseous detector that detects
⁵⁸ charged particle trajectories by measuring the positions and drift time of ions cre-
⁵⁹ ated in the gas. The energies of these particles can be inferred from the curvatures
⁶⁰ of their trajectories in the magnetic field (specific field inside the TPC).

⁶¹ The goal of this thesis is to develop an algorithm for the reconstruction of
⁶² charged particle trajectories and energy in an *atypic* TPC with orthogonal elec-
⁶³ tric and magnetic fields, hereafter referred to as the Orthogonal Fields TPC
⁶⁴ (OFTPC), used in the X17 project at the Institute of Experimental and Applied
⁶⁵ Physics, Czech Technical University in Prague (IEAP CTU). Furthermore, we
⁶⁶ present the results of testing of several (gradually improving) developed algo-
⁶⁷ rithms with different samples of simulated data. Put this somewhere, (maybe
⁶⁸ just the abstract?). We use the Garfield++ toolkit [1] for simulations in combina-
⁶⁹ tion with the ROOT framework [2] for data analysis and visualization. Some of
⁷⁰ our more demanding simulations are run on the MetaCentrum grid [3].

⁷¹ The X17 project in IEAP CTU aims to reproduce measurements of anomalous
⁷² behavior in the angular correlation distribution of pairs produced by the Internal
⁷³ Pair Creation (IPC) mechanism [4] during the decay of certain excited nuclei
⁷⁴ (⁸Be, ¹²C, and ⁴He) observed by a team at ATOMKI in Hungary. I would leave
⁷⁵ this here as a short summary before I explain it in more detail in the sections
⁷⁶ below.

⁷⁷ Add citations: X17 project, VdG. Maybe also TPC, etc.

⁷⁸ 0.1 ATOMKI Anomaly

⁷⁹ Many different theories propose the existence of *new light boson(s)* that are weakly
⁸⁰ coupled to ordinary matter [5]. These particles are potential dark matter candi-
⁸¹ dates and could contribute to a solution of other issues with the Standard Model,
⁸² such as the strong CP problem and the anomalous muon magnetic moment. Mass
⁸³ range of axions?

⁸⁴ A possible way of detecting such bosons with a short lifetime is to observe
⁸⁵ nuclear transitions of excited nuclei. If a boson was emitted during the transition
⁸⁶ and subsequently decayed into an electron-positron pair, we could observe this as
⁸⁷ a peak on top of the standard e^+e^- (both cursive and upright forms are used in
⁸⁸ different articles) angular correlation from the Internal Pair Creation (IPC) and
⁸⁹ the External Pair Creation (EPC).

⁹⁰ 0.1.1 ATOMKI Measurements

⁹¹ Historically, there were several measurements of the IPC in nuclear transitions
⁹² in ⁸Be at Institute für Kernphysik (Frankfurt) [6, 7, 8] and at ATOMKI (De-
⁹³ brecen, Hungary) [9, 10] resulting in different anomalies with invariant mass in
⁹⁴ the range 5 – 15 MeV. This prompted a development of a better spectrometer at
⁹⁵ ATOMKI.

⁹⁶ In 2015, a group at ATOMKI observed an anomalous IPC in ⁸Be [11]. They
⁹⁷ used the ${}^7\text{Li}(p, \gamma){}^8\text{Be}$ reaction at the $E_p = 1030$ keV proton capture resonance

98 to prepare the 18.15 MeV excited state ($J^\pi = 1^+$, $T = 0$). This state decays
99 predominantly through M1 transitions to the ground state ($J^\pi = 0^+$, $T = 0$) and
100 to the 3.03 MeV state ($J^\pi = 2^+$, $T = 0$) [12]. **Transition figure – all transitions
101 of isotopes? IPC figure?**

102 The angular correlation of the e^+e^- pairs created internally in these transitions
103 were measured and compared to the simulation; results from a narrow $E_{\text{sum}} =$
104 = 18 MeV region are shown in Figure 0.1a. The simulation includes boson decay
105 pairs for different boson masses. The disparity parameter y is defined as

$$y = \frac{E_{e^-} - E_{e^+}}{E_{e^-} + E_{e^+}}, \quad (0.1)$$

106 where E_{e^-} and E_{e^+} are the kinetic energies of the electron and positron.

107 Their experimental setup was later upgraded ([details?](#)) and used for new mea-
108 surements. In 2022 the ${}^8\text{Be}$ anomaly was also measured using the $E_p = 441$ keV
109 resonance to produce the 17.64 MeV excited state ($J^\pi = 1^+$, $T = 1$) which again
110 decays primarily to the ground state and the 3.03 MeV state [12]. The anomaly
111 was also measured for $E_p = 650$ and 800 keV where E1 transitions from the direct
112 proton capture dominate [13]. The results for e^+e^- with $E_{\text{sum}} \in [13.5, 20]$ MeV
113 are shown in Figure 0.1b.

114 The newer setup was also used in 2021 to study the ${}^3\text{H}(p, e^+e^-){}^4\text{He}$ reaction at
115 $E_p = 510, 610$ and 900 keV [14], inducing direct and resonant capture populating
116 the overlapping first 20.21 MeV ($J^\pi = 0^+$) and second 21.01 MeV ($J^\pi = 0^-$)
117 excited states [15]. The comparison of simulated and measured e^+e^- pair angular
118 correlations in the $E_{\text{sum}} \in [18, 22]$ MeV region is shown in Figure 0.1c.

119 In 2022, another anomaly was measured in the ${}^{11}\text{B}(p, e^+e^-){}^{12}\text{C}$ process [16].
120 The $E_p = 1388$ keV resonance was used to populate the 17.23 MeV excited state
121 ($J^\pi = 1^-$, $T = 1$) with a large width $\Gamma = 1.15$ MeV [17]. This state decays
122 mainly through E1 transitions to the ground state $J^\pi = 0^+$ and to the 4.44 MeV
123 state $J^\pi = 2^+$. To compensate for energy losses in the target, five energies in
124 the range $E_p = 1.5\text{--}2.5$ MeV were used. The experimental angular correlation for
125 the 17.23 MeV transition to the ground state is shown in Figure 0.1d.

126 Possible explanations of the anomaly include experimental effects, higher or-
127 der processes in the Standard Model [18, 19] or even a protophobic fifth force
128 mediated by a new 17 MeV boson X17 [20]. **Not sure if the introduction should
129 be referenced since even though it is related, it is an independent theory de-
130 veloped only (?) to explain these measurements. Zhang and Miller: <https://www.sciencedirect.com/science/article/pii/S0370269321000010>**

132 0.1.2 Other Experiments

133 Since the ATOMKI measurements, several experiments have been initiated to
134 attempt to replicate the results and search for the hypothetical X17 particle. The
135 following experiments have already produced results. **Could cite the ATOMKI
136 review paper here.**

137 Two-arm e^+e^- spectrometer in Hanoi

138 The anomaly in ${}^8\text{Be}$ has been observed with a high ($> 4\sigma$ **That's all they write
139 in their article.**) confidence by a team at the Hanoi University of Sciences for

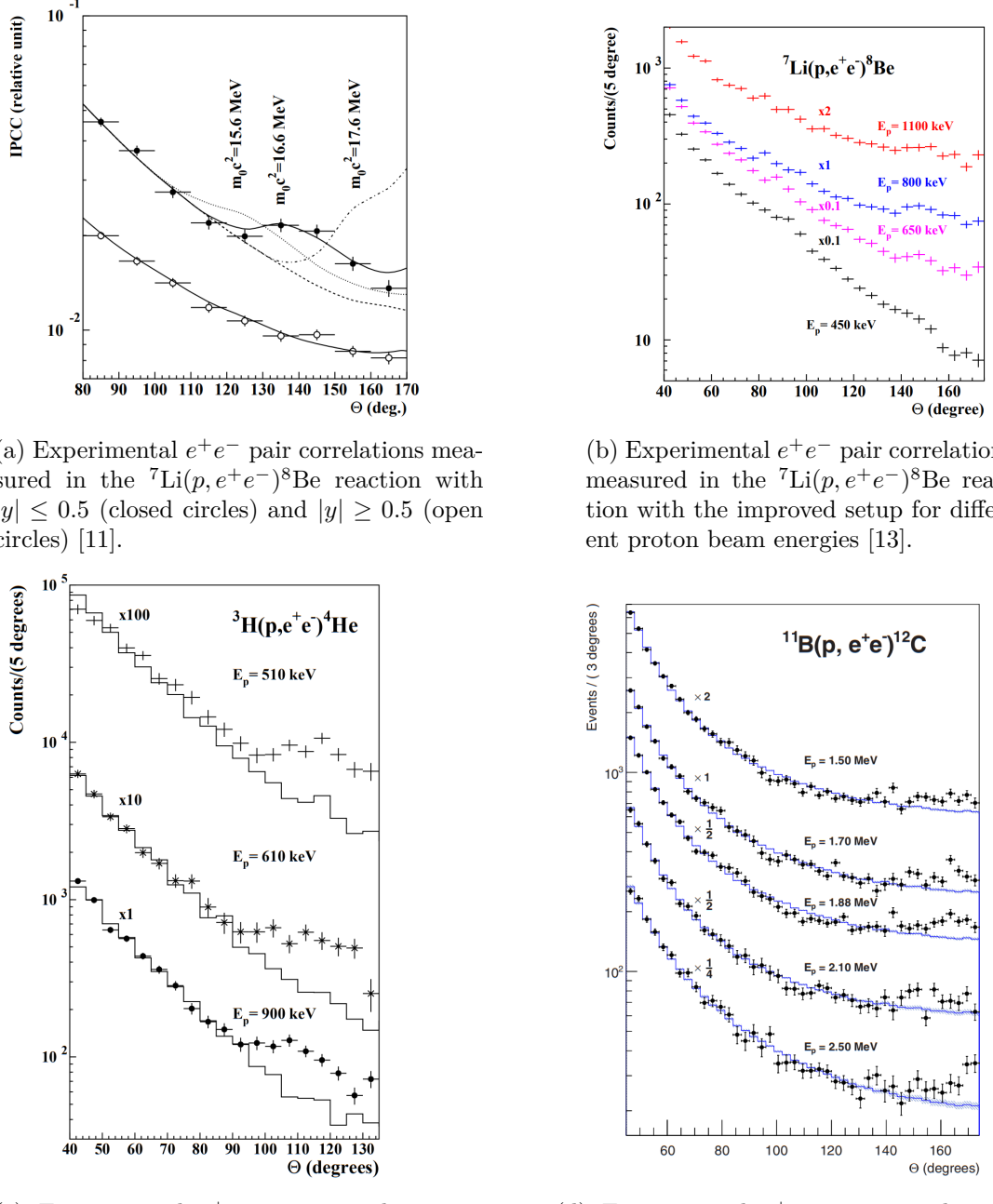


Figure 0.1: The ATOMKI anomalous IPC measured for different nuclei.



Figure 0.2: Results from the Hanoi spectrometer – angular e^+e^- pair correlations measured in the ${}^7\text{Li}(p, e^+e^-){}^8\text{Be}$ reaction at $E_p = 1225$ keV [21].

140 $E_p = 1225$ keV [21]. They built a two-arm spectrometer in collaboration with
141 ATOMKI and calibrated it using the 17.6 MeV M1 transition. The results are
142 shown in Figure 0.2.

143 Collisions at Nuclotron in Dubna

144 At the Joint Institute for Nuclear Research in Dubna, signal in the form of en-
145 hanced structures in the $\gamma\gamma$ spectra at ~ 17 and 38 MeV invariant masses for
146 $p + \text{C}$, $d + \text{C}$ and $d + \text{Cu}$ reactions at momenta 5.5 , 2.75 , and 3.83 GeV per nu-
147 cleon [22]. Monte Carlo simulations support the conclusion that the signals are
148 a consequence of a decay of unknown particles X17 and E38.

149 The MEG II (Muon Electron Gamma) experiment

150 Experiments using the ${}^7\text{Li}(p, e^+e^-){}^8\text{Be}$ reaction were carried out at the Paul
151 Scherrer Institute with the MEG II superconducting solenoid spectrometer [23].
152 Analysis of the data with $E_p = 1080$ keV exciting both of the resonances (beam
153 fully stopping in the target) found no significant evidence supporting the X17
154 hypothesis, results are shown in Figure 0.3. An upper bound (at 90% confidence)
155 on the X17-to- γ branching ratio was set at $1.2 \cdot 10^{-5}$ for the 18.15 MeV state
156 (larger than the ratio $5.8 \cdot 10^{-6}$ obtained by ATOMKI in 2016). Could add their
157 90% C.L bounds figure also. Insufficient statistics – 6.2 % (1.5σ) p-value.

158 0.2 X17 Project at IEAP CTU

159 The aim of the X17 project at the Van der Graaff facility of the Institute of
160 Experimental and Applied Physics, Czech Technical University in Prague is to
161 repeat the original ATOMKI experiments with ${}^7\text{Li}$ and ${}^3\text{H}$ targets using an inde-
162 pendent e^+e^- spectrometer. In order to effectively measure the anomaly, we need
163 to reconstruct both the energy and the angular correlation of the e^+e^- pairs. The

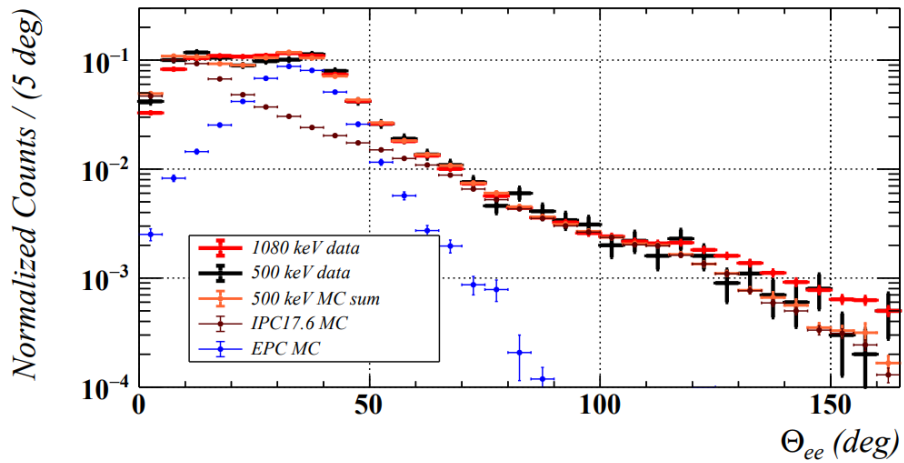


Figure 0.3: Results from the MEG II experiments – angular correlation of e^+e^- pairs with $E_{\text{sum}} \in [16, 20]$ MeV measured in the ${}^7\text{Li}(p, e^+e^-){}^8\text{Be}$ reaction with proton beam energies 500 and 1080 keV. The 500 keV dataset is fitted with Monte Carlo of both the IPC deexcitation and the EPC produced by gammas [23].

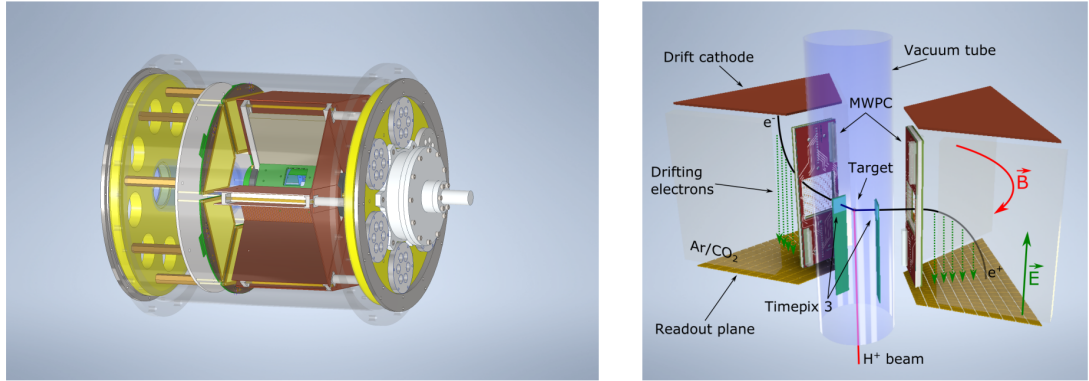


Figure 0.4: Schematics of the detector at the Van der Graaff facility at IEAP CTU.

164 spectrometer will use three layers of detectors to achieve this – Timepix 3 (TPX3)
 165 silicon pixel detector and Multi-Wire Proportional Chamber (MWPC) layers for
 166 the angle reconstruction and a Time Projection Chamber (TPC) layer for the en-
 167 ergy reconstruction. The schematics of the prepared detector is in Figure 0.4
 168 Spectrometer CAD drawing (coordinates here or next chapter?). Cite some VdG
 169 paper, mention grant? Using [https://cernbox.cern.ch/pdf-viewer/public/
 170 rf0oU1nqVLN3acZ/LuzH_submitted.pdf](https://cernbox.cern.ch/pdf-viewer/public/rf0oU1nqVLN3acZ/LuzH_submitted.pdf).

171 The energy of e^+e^- pair produced in the reaction is given by the energy
 172 available E_r in the reaction and can be distributed between them arbitrarily.
 173 Nonetheless in the decay of the hypothetical X17 particle, electron and positron
 174 should have similar energy and we can therefore use a disparity cut $|y| \leq 0.5$
 175 for the disparity parameter (defined in Equation 0.1). Interesting events should
 176 rarely have a particle with an energy below $E_r/4$ (roughly 4 MeV). Electrons with
 177 such low energies are scattered significantly by even a thin layer of relatively light
 178 material, for this reason the TPX3 layer will be inside of the vacuum tube and

179 the tube will have a thinned aluminum segment or KaptonTM windows.

180 TPX3 can measure (in each $55 \times 55 \mu\text{m}$ pixel of its 256×256 grid) time-of-arrival
181 (ToA) with 1.6 ns precision and time-over-threshold (ToT) which reflects the de-
182 posited energy. This potentially allows 3D tracking if we increase the chip thick-
183 ness at the cost of increased scattering. The layer can reconstruct the reaction
184 vertex and the angular correlation with high precision.

185 The layer of MWPCs with sensitive area $40 \times 38 \text{ mm}^2$ will be outside of
186 the beam pipe. It will provide an extra point on the particle trajectory which can
187 help with the estimation of the reaction vertex and improve the TPC performance
188 by providing its entry point.

189 The TPCs, which are a subject of this theses, are in a magnetic field of per-
190 manent magnets positioned between them and provide 3D track reconstruction
191 and subsequent momentum and particle identification (its charge, or even type
192 based on its stopping power). They avoid radiative losses thanks to the small
193 interaction with the incident particle. For the readout, triple Gas Electron Mul-
194 tiplier (GEM) will be used. The magnetic field layout in our TPCs is atypical –
195 orthogonal to the electric field inside the chamber, this is why we call them Or-
196 thogonal Fields TPC (OFTPC). Further details about our OFTPCs are provided
197 in section 1.3.

1. Time Projection Chamber

198 Using (2010 – a little old) <https://cds.cern.ch/record/1302071/files/CERN-PH-EP-2010-047.pdf>

200 A Time Projection Chamber (TPC) is a type of gaseous detector that uses
201 the drift in an electric field of free charges (electrons and cations, **also anions if**
202 **attachment of electrons to the gas particles is considered**) produced by an ionizing
203 particle to reconstruct its 3D trajectory. When placed inside a magnetic field,
204 the momentum of the incident particle can be inferred from the curvature of its
205 trajectory. Particle identification is also possible using the ionization energy loss
206 inside the TPC (see Figure 1.1). The detector used 80:20 Ar:CH₄ mixture at
207 8.5 atm pressure.

208 The original TPC used in the PEP-4 experiment at SLAC (Figure 1.2) was
209 a 2 × 2 m cylinder with a central cathode that produced a strong electric field,
210 making the ionization electrons drift towards one of the bases. The readout
211 consisted of MWPCs, where electrons are accelerated towards the anode wires
212 enough to further ionize the gas and cause an avalanche.

213 When a charged particle crosses the volume of a TPC, it loses energy by ex-
214 citation and ionization of the detector gas (**how much – from dE/dx + density**
215 → **footnote?**). Most ionizing collision produce a single ionization electron, some-
216 times a few secondary electrons are produced close to the collision vertex. In
217 rare cases, the ionization electron has energy large enough to create a measurable
218 track, such an electron is called a δ -electron (**terminology, just like below – tech-**
219 **nically it's a (primary) ionization electron causing other (secondary) ionization**).
220 Penning transfer (collisions, light – factor 10 for gas gain in Ar/CO₂ viz PDG
221 CERN)?

222 CERES/NA45 – very inhomogeneous magnetic field

223 1.1 Charge transport in gases

224 1.1.1 Drift

225 Produced ionization electrons (**terminology – called ionization electrons in the rest**
226 **of the thesis, ionoelectrons?**) are accelerated towards the readout by the electric
227 field inside the chamber. At the same time, they lose speed by colliding with
228 the gas particles, quickly reaching a constant (for a given field \mathbf{E}, \mathbf{B}) mean drift
229 velocity. The electrons might be absorbed by electronegative impurities, such as
230 halides and oxygen.

231 In many gases (called "hot", e.g., Ar or CH₄), the drift velocity (**def? the**
232 **paragraph above not enough?**) is much greater than that of their thermal motion
233 thanks to a high proportion of elastic collisions. On the other hand, "cold"
234 gases like CO₂ have a higher proportion of inelastic collisions (e.g., thanks to
235 the excitation of rotational and vibrational states) and therefore much lower
236 (**value? magnitude (implied)?**) drift velocity.

237 The ions produced by the ionization lose a significant portion of their energy
238 during each collision since their mass is close to the mass of the gas particles (**see**
239 **the source material – average energy loss during collision** $\Delta E = \frac{2m_i M}{(m_i + M)^2}$, this way
240 it's more accurate). This, together with their large collision cross section, makes

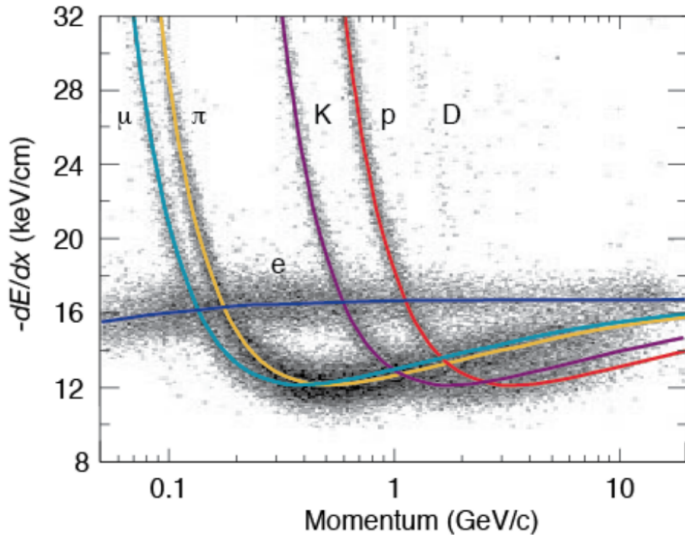


Figure 1.1: Particle identification in the PEP-4 TPC at SLAC based on the energy loss per distance $\frac{dE}{dx}$ [24].

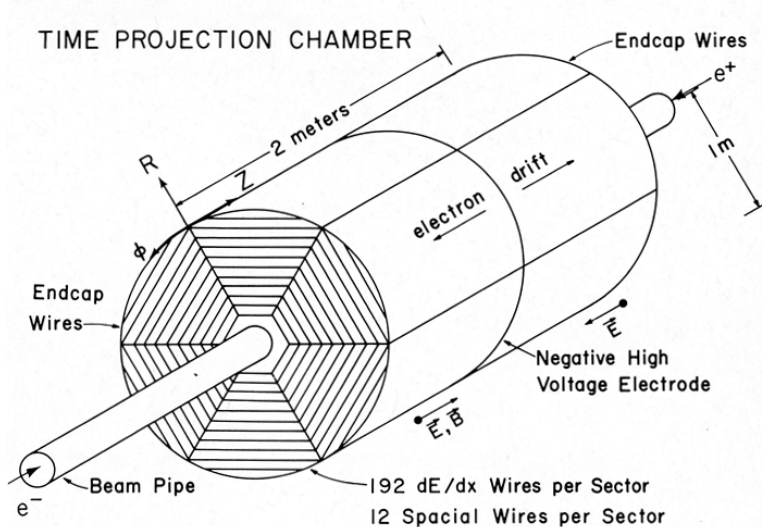


Figure 1.2: Schematic view of the PEP-4 TPC [25]. A charged particle produced in a collision in the beam pipe creates a spiral ionization track in the magnetic field. The central cathode then accelerates ionization electrons towards the endcap anode wires where they are multiplied and read out.

their drift velocity much smaller and their energy is close to thermal. Since their momenta aren't randomized to such an extent during collisions, their diffusion is smaller (**more in the sense of distribution of positions, could move this to the diffusion subsection**).

The drift is also influenced by the magnetic field. Langevin derived a good approximation for the drift velocity vector:

$$\mathbf{v}_d = \left(\frac{\mathbf{E}}{\|\mathbf{E}\|} + \omega\tau \frac{\mathbf{E} \times \mathbf{B}}{\|\mathbf{E}\| \|\mathbf{B}\|} + \omega^2\tau^2 \frac{\mathbf{E} \cdot \mathbf{B}}{\|\mathbf{E}\| \|\mathbf{B}\|} \cdot \frac{\mathbf{B}}{\|\mathbf{B}\|} \right) \frac{q\tau}{m(1 + \omega^2\tau^2)} \|\mathbf{E}\|, \quad (1.1)$$

where q is the charge of the particle, m is its mass, τ is the mean time between collisions and $\omega = \frac{q}{m} \|\mathbf{B}\|$ is the Larmor frequency. In a standard TPC, \mathbf{E} is nearly parallel to \mathbf{B} and the influence of the magnetic field on the drift is minimal. The drift of ions is only negligibly influenced by the magnetic field ($\omega\tau \sim 10^{-4}$ is small due to the low drift velocity – better because it takes τ into account and differs only by E/B ratio). Lorentz angle for orthogonal fields $\tan \psi = -\omega\tau$ (deviation from electric field) – mention in the OFTPC section. Without magnetic field, we can write

$$\mathbf{v}_d = \frac{q\tau}{m} \mathbf{E} = \mu \mathbf{E}, \quad (1.2)$$

where μ is called charge mobility.

1.1.2 Diffusion

Due to collisions a cloud of electrons or ions originating from the same point will show a Gaussian density distribution at time t while drifting in the electric field $\mathbf{E} = (0, 0, E_z)$ along the z -coordinate (**coordinates defined by the electric field**):

$$\rho(x, y, z, t) = (4\pi Dt)^{-\frac{3}{2}} \exp\left(-\frac{x^2 + y^2 + (z - v_d t)^2}{4Dt}\right), \quad (1.3)$$

where the diffusion coefficient D can be expressed as

$$D = \frac{\lambda^2}{3\tau} = \frac{\lambda v_d}{3} = \frac{v_d^2 \tau}{3} = \frac{2\varepsilon\tau}{3m}, \quad (1.4)$$

where λ is the mean free path and ε the mean energy. The lateral diffusion width σ_x after a drift distance L can be expressed as

$$\sigma_x^2 = 2Dt = \frac{4\varepsilon L}{3qE}. \quad (1.5)$$

The minimal diffusion width is given by the lowest possible energy of the particles $\varepsilon_{\text{th}} = \frac{3}{2}kT$ (corresponding to thermal motion):

$$\sigma_{x, \text{min}}^2 = \frac{2kTL}{qE}. \quad (1.6)$$

For electrons in "cold gases" (e.g., Ar/CO₂ mixture), the diffusion approaches this limit up to a certain field intensity (~ 100 V/cm at 1 atm pressure)¹. In

¹For us $\sigma_{x, \text{min}} = 0.45$ mm, quite close to the actual diffusion 0.5-0.7 mm – details of the calculation.

267 reality, the transversal diffusion of electrons can differ significantly from their
268 longitudinal diffusion and simulations are necessary to get a precise result.

269 In most TPCs, the transversal (but not the longitudinal) diffusion is reduced
270 by the magnetic field, since it is parallel to the electric field and curves the dif-
271 fusing electrons around their mean trajectory:

$$\frac{D_T(B)}{D_T(0)} = \frac{1}{C + \omega^2 \tau_2^2}, \quad (1.7)$$

272 where C and τ_2 are parameters dependent on the gas used. At low intensity of
273 the magnetic field, we can use an approximation $C \approx 1$ and $\tau_2 \approx \tau$.

274 1.2 Readout

275 1.2.1 Multi-Wire Proportional Chamber

276 In most (2010 – almost all) TPCs operated in experiments Multi-Wire Pro-
277 portional Chamber (MWPC) (actually wire chamber – similar) was used for the read-
278 out. The electrons enter the chamber through a cathode grid and get accelerated
279 in the strong electric field towards the thin anode wires and create a Townsend
280 avalanche (ref), multiplying the signal. Alternating with field wires? That is the
281 difference between MWPC and a drift chamber? The trajectory can be recon-
282 structed using signal from each separate wire. Segmented cathode is also often
283 used for the readout of produced cations. Gating grid (reduction of space charge
284 effect, blocking backflow of ions?, closed for electrons $B=0$, ΔV , static mode (loss
285 of 25% el.) x opening on trigger)? (gas amplification > 10000 required for good
286 SNR, 100-200 ns shaping time), figure – field (acts as a plane from far away and
287 the field only gets strong enough for avalanches)?

288 1.2.2 Gas Electron Multiplier

289 A Gas Electron Multiplier (GEM) is a thin metal-coated polymer sheet with
290 a high density of small holes (Figure 1.3). The amplification is achieved by ap-
291 plying voltage on the metal layers, creating a strong electric field inside the holes
292 and causing avalanches (see Figure 1.4). Double or triple stack of GEMs is usu-
293 ally used to create a sufficient gain. From the last foil, the electrons drift to
294 a segmented anode where the signal is read. The backflow of cations is reduced
295 compared to MWPC. Typical parameters (vs thick GEM?).

296 1.2.3 Micromegas

297 In a MICRO-MEsh GAseous Structure (Micromegas) (in sources I viewed it is not
298 capitalized) electrons pass through a fine mesh (made out of very thin wires) into
299 the narrow amplification gap where they are multiplied in the high field and read
300 as signal on the segmented anode. Very high field ($30\text{-}80 \text{ kV/cm}^2$) is necessary
301 to achieve sufficient gain. Cation backflow is heavily suppressed by the mesh.

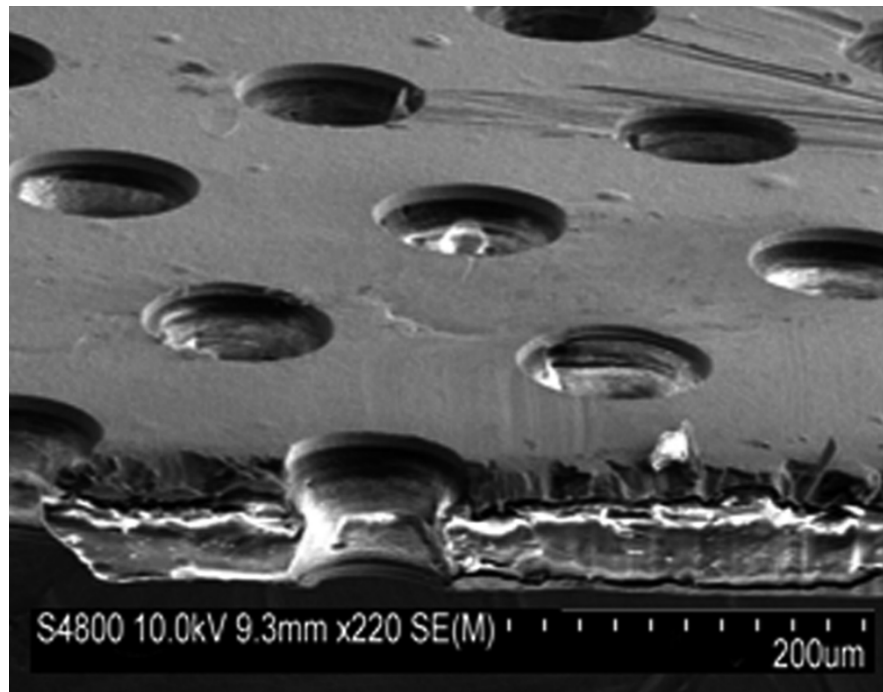


Figure 1.3: A scanning electron microscope image of a GEM foil.

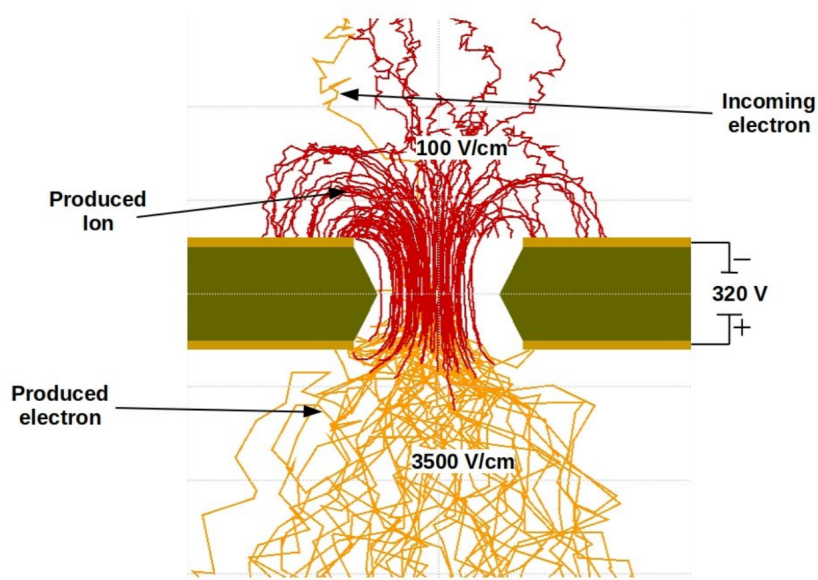


Figure 1.4: Garfield simulation of an avalanche in a GEM hole [26]. An incoming electron (orange) is accelerated in the strong electric field of the GEM and causes further ionization multiplying the number of free electrons (orange). Most of the produced cations (red) are captured by the GEM cathode.

302 **1.2.4 Parallel Plate Chamber**

303 ... micowell? – these readouts and Micromegas are not used in our detector,
304 so maybe just mention them at the beginning of the readout section without
305 excessive detail (some subfigures showing how they look without describing each
306 too much)

307 **1.3 Orthogonal Fields TPC at IEAP CTU**

308 At IEAP CTU, we are going to use six identical atypical TPCs with inhomogeneous
309 toroidal magnetic field **orthogonal** to the electric field (**details below**),
310 hereafter referred to as Orthogonal Fields TPC (OFTPC). It has the shape of
311 isosceles trapezoidal prism 16 centimeters high with triple-GEM readout on one
312 of its bases. Dimensions of the OFTPC are discussed in detail in section 1.3.2
313 below. Throughout this thesis, we assume a uniform electric field along the z axis
314 with $E_z = -400 \text{ V/cm}$. **Gas mixture used in the detector (70/30) and its effect**
315 – some graph with the mixture.

316 **1.3.1 Motivation and Associated Challenges**

317 The reasons for the unusual field layout are mostly cost related:

- 318 a) we use permanent magnets instead of a solenoid and parallel fields are
319 difficult to accomplish this way,
- 320 b) granularity of the TPC readout is limited in order to fit one SAMPA/SRS
321 hybrid in each sector – parallel fields would bend the trajectories parallel
322 to the readout requiring more pads and different architecture.

323 In this thesis, we will show that such a setup can reach a similar energy resolution
324 as common cylindrical TPCs while reducing the overall cost.

325 The layout introduces two complications to the track reconstruction – the
326 trajectory in inhomogeneous field is not circular and the drift is distorted by the
327 magnetic field as shown in the Equation 1.1(in our case $\omega\tau \approx 0.08$ **for 0.3 T**
328 **assuming $\mu \approx 0.25 \text{ T}^{-1}$, varies inside the detector**). We will deal with these
329 effects in the upcoming chapters.

330 The diffusion in such setup is larger since parallel orientation reduces diffusion
331 by curling the electrons in the x - y direction (see Equation 1.7), but for our
332 relatively weak magnetic field and short drift distance, the difference is negligible.

333 **1.3.2 Coordinate Systems and Dimensions**

334 In order to describe events in our detector, we use three distinct spaces: the de-
335 tector space \mathcal{D} , the readout space \mathcal{R} and the pad space \mathcal{P} (**different spaces that**
336 **describe different things and each has their own coordinate system, so maybe**
337 **rename the section somehow?**). Each space is later used to represent ionization
338 electrons at different stages of the detection process: their creation in the gas,
339 their final position when hitting the readout plane, and finally their representation
340 in the discrete pad space.

341 **Detector Space**

342 The detector space \mathcal{D} represents the physical space of our detector. We de-
343 scribe it using Cartesian coordinates (x, y, z) . The z -axis is the detector's axis of
344 symmetry, with its negative direction aligned with the proton beam. The origin
345 $(0, 0, 0)$ is located at the center of the irradiated target. The positive x -axis passes
346 through the center of one the OFTPCs along the intersection of its two planes
347 of symmetry. The y -axis is then chosen to maintain a right-handed coordinate
348 system.

349 Since the detector has a hexagonal symmetry, we use only one of its sectors
350 in this work – the first sector $\mathcal{D}_1 \subset \mathcal{D}$ which is defined by the condition:

$$(x, y, z) \in \mathcal{D}_1 \Leftrightarrow |y| \leq x \tan \frac{\pi}{6}. \quad (1.8)$$

351 Simulations in this sector can be applied to all sectors by rotating the coordinates
352 accordingly. The volume of the OFTPC in this sector, which has the shape of
353 a trapezoidal prism, has these boundaries:

$$x \in [x_{\min}, x_{\max}] = [6.51, 14.61] \text{ cm}, \quad (1.9)$$

$$z \in [z_{\min}, z_{\max}] = [-8, 8] \text{ cm}, \quad (1.10)$$

$$y_{\max}(x_{\min}) = -y_{\min}(x_{\min}) = 2.75 \text{ cm}, \quad (1.11)$$

$$y_{\max}(x_{\max}) = -y_{\min}(x_{\max}) = 7.45 \text{ cm}, \quad (1.12)$$

354 where $y_{\max}(x)$ is the maximal value of the y -coordinate for a given x . The read-
355 out is located at $z = 8$ cm; for some purposes, we also define the distance to
356 the readout $d_r = 8 \text{ cm} - z$ as an alternative to the z -coordinate. **Keeping this**
357 **paragraph as it is because the OFTPC volume is distinct from the first sector**
358 **and some parts of this thesis use the space beyond this volume.**

359 We also use spherical coordinates (r, θ, φ) with θ measured relative to the xy
360 plane.

361 **Readout Space**

362 The readout space \mathcal{R} represents the drift time and final positions of ionization
363 electrons as measured by an ideal continuous readout. We describe it using
364 coordinates (x', y', t) , where x' and y' correspond to the detector coordinates at
365 the readout plane ($z = 8$ cm).

366 **Currently not entirely sure how to put this into a figure since only x' and**
367 **y' correspond to the detector coordinates, it will make more sense when**
368 **visualizing the map.** The drift time t is approximately proportional to d_r .

369 **Pad Space**

370 The pad space \mathcal{P} represents the time bin and pad number of ionization electrons
371 as measured by an ideal discrete readout:

$$\mathcal{P} = \{(n_{\text{pad}}, n_t) \in \mathbb{N}^2 \mid n_{\text{pad}} \leq 128\}. \quad (1.13)$$

372 **Rewrite to reflect this:** Technically both values can be zero as defined in
373 the code (max channel 127). It is not really a subspace of \mathcal{R} but there is a

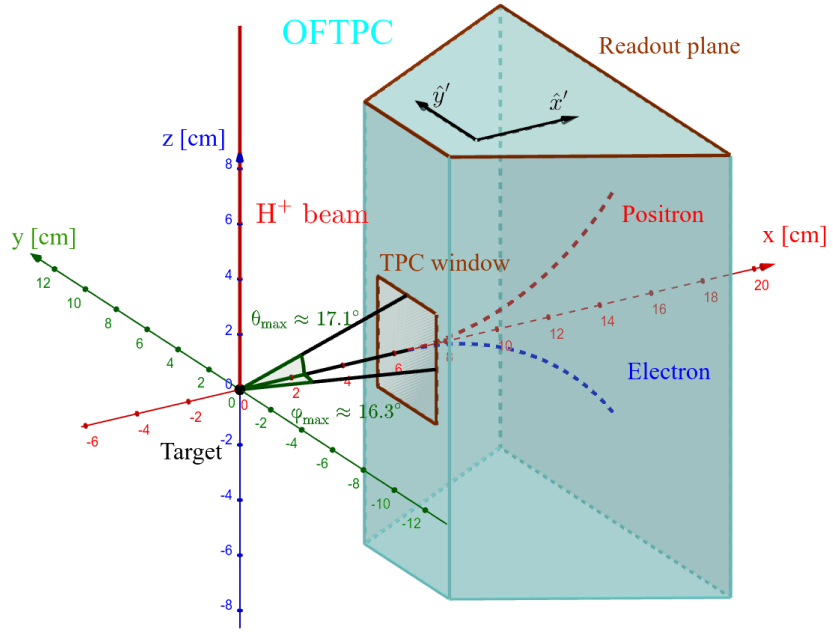


Figure 1.5: Schematics of the first sector OFTPC with detector space coordinates.

374 mapping from \mathcal{R} to \mathcal{P} . It is a discretization of a part of \mathcal{R} , the mapping can be
 375 adjusted depending on the simulation. If we assume uniform electric field there
 376 will be gaps, we don't use gaps in the reconstruction since the electrons should
 377 be pulled towards the pads.

378 The readout of the OFTPC will consist (is the design final?) of 128 rectangular
 379 pads arranged in a staggered pattern. Parameters of the pad layout are shown
 380 in Figure 1.6. The bottom left corner of n -th pad has coordinates $(x_{1,n}, y_{1,n})$,
 381 the top right $(x_{2,n}, y_{2,n})$ and its center has coordinates $(x_{c,n}, y_{c,n})$. The gap
 382 between neighboring pads is $g = 0.08$ cm. Time will be read out in discrete bins
 383 of size $t_{\text{bin}} = 100$ ns (details?). Could also describe pad-related functions.

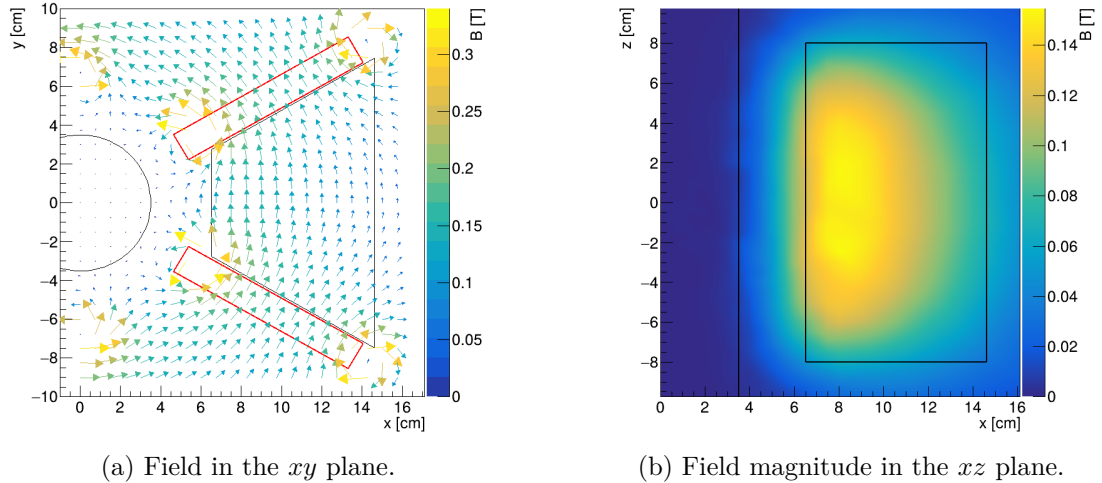


Figure 1.7: Magnetic field simulation results. The OFTPC volume and the vacuum tube are marked with black lines, the magnets are marked with red lines. The coordinates of the magnets from the CAD drawing seem to be 9/10 of the ones from the magnetic simulation (confirm and fix).

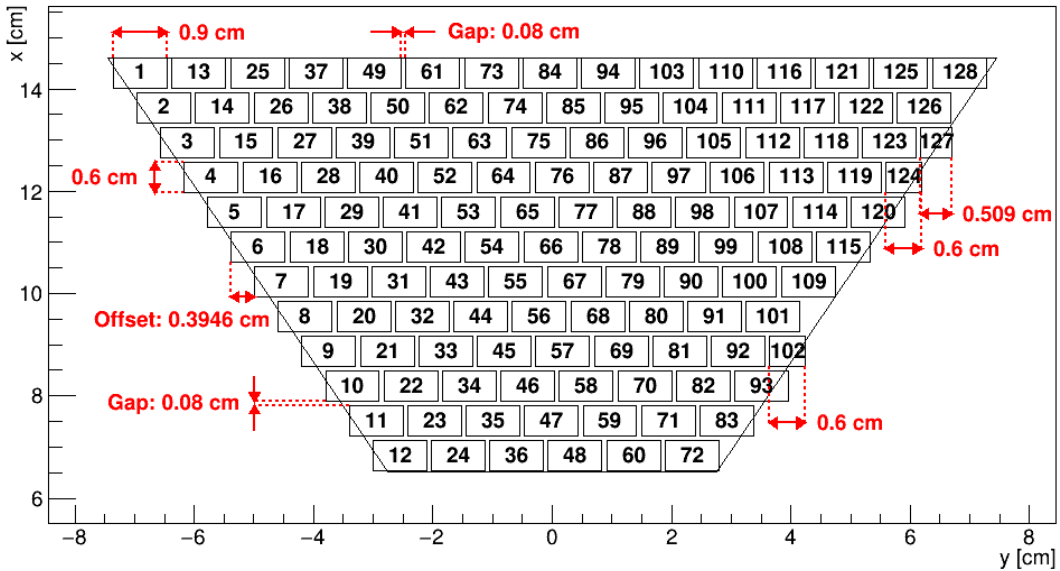


Figure 1.6: Pad layout of the OFTPC and its parameters. Pads 102, 124 and 127 are irregular, the rest has the same dimensions.

384 1.3.3 Magnetic Field Simulation

385 The magnetic field inside our detector is produced by six permanent magnets. It
 386 was simulated using Ansys Maxwell ([citation](#)) which gives us values on a regular
 387 grid. [More details, vacuum tube, magnets \(homogeneous?, density?\)](#). Visualization
 388 of the magnetic field is shown in Figure 1.7. Whenever we need to work with
 389 values outside this grid, we use trilinear interpolation described below.

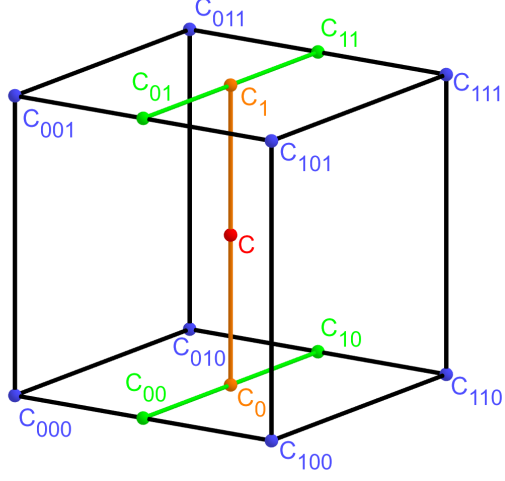


Figure 1.8: Visualization of trilinear interpolation as a composition of linear interpolations (inspired by [27]). We want to interpolate the value in the red point \mathbf{C} . First we interpolate between the four pairs of blue points sharing the last two indices along the x -axis (Eq. 1.14), then between the two pairs of the resulting green points along the y -axis (Eq. 1.15) and finally between the two resulting orange points along the z -axis to get the final red value (Eq. 1.16).

390 Trilinear Interpolation

391 Trilinear interpolation is a 3D generalization of linear interpolation². It can be
 392 used to interpolate a function whose values are known on a regular grid with
 393 rectangular prism cells. We use this simple method for interpolating the magnetic
 394 field, and it is later used in Section 3.2.1 to interpolate the Ionization Electron
 395 Map, a key component of our track reconstruction algorithm. In both cases, we
 396 use a regular cubic grid (apparently it is also called a **Cartesian grid**).

397 Let us consider a cell of our regular grid (a cube) with an edge of length a
 398 containing the point $\mathbf{C} = (x, y, z)$ where we want to interpolate a function
 399 $f: \mathbb{R}^3 \rightarrow \mathbb{R}$. We know the values of this function at the vertices of the cell
 400 $\mathbf{C}_{ijk} = (x_0 + ia, y_0 + ja, z_0 + ka)$, where $\mathbf{C}_{000} = (x_0, y_0, z_0)$ is the origin of the cell
 401 (is that clear?), and $i, j, k \in \{0, 1\}$ are indices. We also define the points $\mathbf{C}_{ij} =$
 402 $= (x, y_0 + ia, z_0 + ja)$ and $\mathbf{C}_i = (x, y, z_0 + ia)$. Then the interpolated value $\hat{f}(\mathbf{C})$
 403 can be calculated as a composition of three linear interpolations (see Figure 1.8):

$$\hat{f}(\mathbf{C}_{ij}) = (1 - x_d) f(\mathbf{C}_{0ij}) + x_d f(\mathbf{C}_{1ij}), \quad (1.14)$$

$$\hat{f}(\mathbf{C}_i) = (1 - y_d) \hat{f}(\mathbf{C}_{0i}) + y_d \hat{f}(\mathbf{C}_{1i}), \quad (1.15)$$

$$\hat{f}(\mathbf{C}) = (1 - z_d) \hat{f}(\mathbf{C}_0) + z_d \hat{f}(\mathbf{C}_1), \quad (1.16)$$

404 where x_d , y_d , and z_d are given as follows:

$$x_d = \frac{x - x_0}{a}, \quad y_d = \frac{y - y_0}{a}, \quad z_d = \frac{z - z_0}{a}. \quad (1.17)$$

²Linear interpolation in point $x \in (x_1, x_2)$ of a function $f: \mathbb{R} \rightarrow \mathbb{R}$ known in points $x_1 < x_2$ is the convex combination $\hat{f}(x) = (1 - x_d)f(x_1) + x_d f(x_2)$, where $x_d = \frac{x - x_1}{x_2 - x_1} \in (0, 1)$.

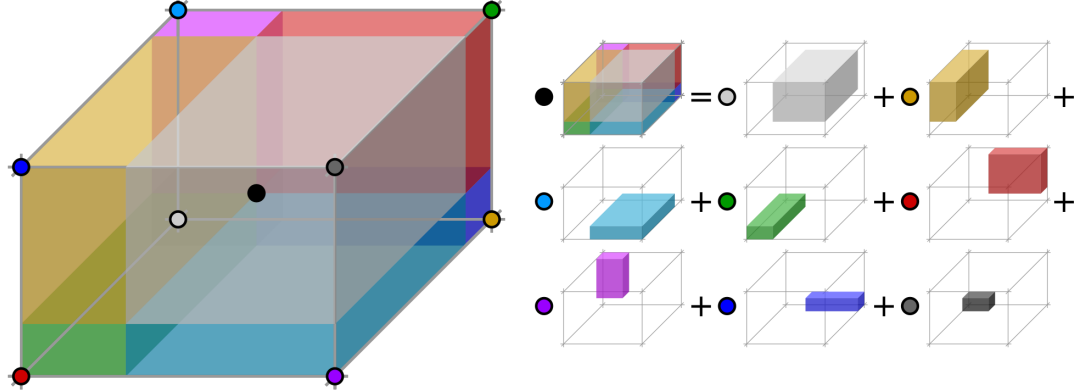


Figure 1.9: Geometric interpretation of trilinear interpolation as expressed in Equation 1.18. The colored dots represent the values in given points and the colored boxes represent the volume in the opposite corner by which the corresponding values are multiplied. The black dot represents the interpolated value which is multiplied by the entire volume [28].

405 We can also write

$$\hat{f}(\mathbf{C}) = \sum_{i,j,k \in \{0,1\}} t_x^i t_y^j t_z^k f(\mathbf{C}_{ijk}), \quad (1.18)$$

$$t_\alpha \stackrel{\text{def}}{=} \begin{pmatrix} t_\alpha^0 \\ t_\alpha^1 \end{pmatrix} = \begin{pmatrix} 1 - \alpha_d \\ \alpha_d \end{pmatrix}, \quad (1.19)$$

406 where $\alpha \in \{x, y, z\}$ is an index. This gives a nice geometric interpretation to the
 407 trilinear interpolation as shown in Figure 1.9. From this form and the figure, it
 408 is apparent that the final interpolated value does not depend on the order of axes
 409 along which we perform linear interpolations (see Figure 1.8). Furthermore, we
 410 can write $\hat{f}(\mathbf{C})$ as a polynomial:

$$\hat{f}(\mathbf{C}) = \sum_{\alpha,\beta,\gamma \in \{0,1\}} \sum_{i=0}^{\alpha} \sum_{j=0}^{\beta} \sum_{k=0}^{\gamma} (-1)^{(\alpha-i)+(\beta-j)+(\gamma-k)} f(\mathbf{C}_{ijk}) x_d^\alpha y_d^\beta z_d^\gamma. \quad (1.20)$$

411 We take advantage of this form when generalizing trilinear interpolation to irreg-
 412 ular grid in section 3.2.2.

413 Maybe a citation here, although I am not sure it is necessary since it could
 414 be considered common knowledge. The last two equations are my own (but I'm
 415 not sure that's worth mentioning unless there's a citation).

2. Track Simulation

In order to develop and test the reconstruction algorithm, electron and positron tracks are simulated inside the first detector sector \mathcal{D}_1 (see Section 1.3.2) with different initial parameters (origin, initial direction and kinetic energy). Two approaches are currently used to simulate tracks, each of them for different purpose.

The **Microscopic Simulation** uses the Garfield++ toolkit [1]. Within this toolkit:

- a) Magboltz, since it is mentioned later
- b) the High Energy Electro-Dynamics (HEED) program [29] is used to simulate the primary particle,
- c) the class *AvalancheMicroscopic* to simulate the drift of secondary electrons created by ionization in the gas.

This is the most precise and time-consuming simulation used; our current goal is to be able to successfully reconstruct its results and determine our best-case energy resolution.

The **Runge-Kutta Simulation** uses the 4th order Runge-Kutta numerical integration (add citation for Runge-Kutta) to simulate the trajectory of the primary particle in the electromagnetic field inside the detector. It is relatively fast since it does not simulate the secondary particles. It is used as part of our reconstruction algorithm and for testing some parts of the reconstruction.

All of these simulations require the knowledge of the electromagnetic field (both **E** and **B**) inside the detector. A uniform electric field of $400 \text{ V}\cdot\text{cm}^{-1}$ is assumed. The magnetic field was simulated in Maxwell (see Section 1.3.3). add citation

Single track in positive x direction or initial parameter randomization. Importance of gas composition, used gas compositions.

2.1 Microscopic Simulation

The microscopic simulation, the most detailed simulation used in this work, is performed using the Garfield++ toolkit [1].

The electron transport properties are simulated using the program Magboltz (add citation, details?). Two different gas mixtures were compared – 90:10 and 70:30 Ar:CO₂. The second mixture will be used in our detector (this was probably known a priori, but the first tests that I started with used 90/10, so maybe just note that the results justify the fact so far). The temperature is set to 20 °C, the pressure is atmospheric.

The primary track is simulated using the program HEED, which is an implementation of the photo-absorption ionization model [29] (see the reference, moved it to the end of sentence). This program provides the parameters of ionizing collisions. HEED can also be used to simulate the transport of delta electrons; we do not account for these in the current simulation (but plan to include them in the future – maybe mention only in the conclusion/future section). The photons created in the atomic relaxation cascade (fluorescence reabsorption, ?) are also not simulated.

459 Finally, we use the microscopic tracking provided by the class *AvalancheMicroscopic*
 460 in Garfield++ to simulate the drift of the ionization electrons. Each
 461 electron is followed from collision to collision using the equation of motion and
 462 the collision rates calculated by Magboltz.

463 First simulated track in the z direction should be described in detail here (own
 464 subsection of the microscopic section, together with a subsection for random/grid
 465 batches?). Figures.

466 Add more detailed and better description of HEED, and microscopic tracking
 467 (each their own subsection?). Could also mention Monte Carlo (requires gas file
 468 generation - Magboltz) and Runge-Kutta simulation implemented in Garfield,
 469 why we don't use them (another subsection? rename the section to Garfield++
 470 simulation and mention all relevant parts?).

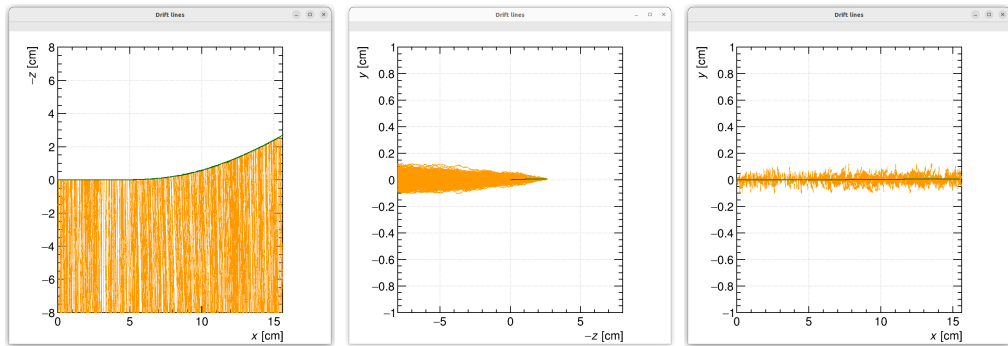


Figure 2.1: Example of a simulated electron track in 70 % argon and 30 % CO₂ atmosphere (on the left). Swap for better images, better zoom. Explain drift lines, primary particle.

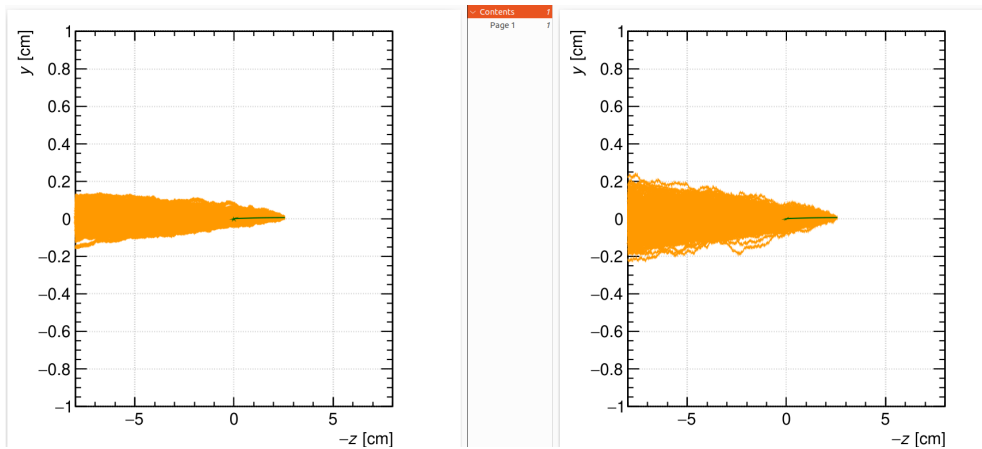


Figure 2.2: Comparison of diffusion in a simulated electron track in 70 % argon, 30 % CO₂ atmosphere and in 90 % argon, 10 % CO₂ atmosphere (on the right). Swap for better image, better zoom. Or put the same pictures for both comparisons in one subfigure, etc. Describe better.

2.2 Runge-Kutta Simulation

471 The Runge-Kutta simulation in this work uses the Runge-Kutta 4th order (RK4)
 473 method to numerically integrate the equation of motion of a relativistic charged
 474 particle in an electromagnetic field. Given a system of first order differential
 475 equations

$$\frac{dy}{dt} = \mathbf{f}(t, \mathbf{y}(t)) \quad (2.1)$$

476 with an initial condition

$$\mathbf{y}(t_0) = \mathbf{y}_0, \quad (2.2)$$

477 we iteratively compute the estimate $\mathbf{y}_n = \mathbf{y}(t_n) = \mathbf{y}(t_0 + nh)$ as follows ([citation?](#)
 478 [common knowledge?](#)):

$$\mathbf{k}_1 = \mathbf{f}(t_n, \mathbf{y}_n), \quad (2.3)$$

$$\mathbf{k}_2 = \mathbf{f}\left(t_n + \frac{h}{2}, \mathbf{y}_n + \frac{h\mathbf{k}_1}{2}\right), \quad (2.4)$$

$$\mathbf{k}_3 = \mathbf{f}\left(t_n + \frac{h}{2}, \mathbf{y}_n + \frac{h\mathbf{k}_2}{2}\right), \quad (2.5)$$

$$\mathbf{k}_4 = \mathbf{f}(t_n + h, \mathbf{y}_n + h\mathbf{k}_3), \quad (2.6)$$

$$\mathbf{y}_{n+1} = \mathbf{y}_n + \frac{1}{6}(\mathbf{k}_1 + 2\mathbf{k}_2 + 2\mathbf{k}_3 + \mathbf{k}_4). \quad (2.7)$$

480 Alternate forms (infinitely many) possible, accuracy vs computational cost. Runge-
 481 Kutta-Fehlberg with adaptive step size also possible, can potentially save some
 482 computation time especially in rapidly changing field (so maybe not in this case).

483 In our case, we want to integrate the equation of motion, given by the rela-
 484 tivistic Lorentz force:

$$F_L^\mu = m \frac{du^\mu}{d\tau} = q F^{\mu\nu} u_\nu, \quad (2.8)$$

485 where the Einstein summation convention is used, m is the mass of the particle,
 486 q is its charge, u^μ is its four-velocity, τ is the proper time (i.e., time in the particle's
 487 frame of reference) and $F^{\mu\nu}$ is the electromagnetic tensor at given coordinates x^μ
 488 (we consider it to be time-independent in our detector). Given the electric $\mathbf{E} =$
 489 $= (E_x, E_y, E_z)$ and the magnetic field $\mathbf{B} = (B_x, B_y, B_z)$ and using the metric
 490 signature $(+, -, -, -)$, the equation expands to

$$\frac{d}{d\tau} \begin{pmatrix} \gamma c \\ \gamma v_x \\ \gamma v_y \\ \gamma v_z \end{pmatrix} = \frac{q}{m} \begin{pmatrix} 0 & -\frac{E_x}{c} & -\frac{E_y}{c} & -\frac{E_z}{c} \\ \frac{E_x}{c} & 0 & -B_z & B_y \\ \frac{E_y}{c} & B_z & 0 & -B_x \\ \frac{E_z}{c} & -B_y & B_x & 0 \end{pmatrix} \begin{pmatrix} \gamma c \\ \gamma v_x \\ \gamma v_y \\ \gamma v_z \end{pmatrix}, \quad (2.9)$$

491 where c is the speed of light in vacuum, $\mathbf{v} = (v_x, v_y, v_z)$ is the particle's velocity
 492 and $\gamma = (1 - \frac{v^2}{c^2})^{-\frac{1}{2}}$ is the Lorentz factor ([wrong magnetic field sign in the](#)
 493 [implementation???](#)). Together with the equation

$$\frac{d}{d\tau} \begin{pmatrix} ct \\ x \\ y \\ z \end{pmatrix} = \begin{pmatrix} \gamma c \\ \gamma v_x \\ \gamma v_y \\ \gamma v_z \end{pmatrix} = u^\mu, \quad (2.10)$$

494 we get a system of eight first order differential equations for x^μ and u^μ , which
 495 we can integrate using the Runge-Kutta method described above. As a result of
 496 this integration, we get the position $\mathbf{x}(\tau_n)$, the velocity $\mathbf{v}(\tau_n)$ and the detector
 497 time $t(\tau_n)$ for every proper time $\tau_n = n\tau_{\text{step}}$. Integrating using the proper time
 498 means, that the step size in t gets larger by the gamma factor $\frac{dt}{d\tau} = \gamma$ (maybe
 499 change it and integrate the detector time or adjust the step size accordingly). The
 500 only difference is in the step size (because t gets also calculated as it is among
 501 the 8 variables) As initial conditions, we use the origin of the track (x_0, y_0, z_0) ,
 502 the initial velocity direction vector $\mathbf{n} = (\cos \varphi \cos \theta, \sin \varphi \cos \theta, \sin \theta)$ and the ki-
 503 netic energy E_{kin} (initial parameters of the simulation (fit is in chapter 4)), we
 504 then compute γ and $\|\mathbf{v}\|$:

$$\gamma = 1 + \frac{E_{\text{kin}}}{E_0}, \quad (2.11)$$

$$\|\mathbf{v}\| = c\sqrt{1 - \gamma^{-2}}. \quad (2.12)$$

505 Example of RK simulation – first testing track, randomized sample of 100000
 506 tracks.

3. Track Reconstruction

508 As the first step of the reconstruction algorithm, we reconstruct the track of
509 a primary particle – either an electron or a positron. Then, using this information,
510 we determine the energy of the particle (Section 4).

511 The **Reconstruction Assuming Steady Drift** uses the standard TPC ap-
512 proach. With parallel fields, the drift inside a uniform electric field remains
513 undistorted (as shown in Equation 1.1). Therefore, we only need to reconstruct
514 the z -coordinate from the drift time using the known drift velocity. We also
515 assume that the readout coordinates (x' , y' , t) are known exactly, neglecting
516 the pads and time binning.

517 Reconstruction using an **Ionization Electron Map** (from now on referred
518 to as *the map*) uses a simulation of the drift of secondary (ionization) electrons
519 within the detector volume. This simulation can then be used to interpolate
520 the initial position of the secondary electrons. In the first iteration of this method
521 the readout is assumed to be continuous.

522 We present two algorithms using the map for reconstruction. The first one uses
523 a gradient descent algorithm along with trilinear interpolation (see Section 1.3.3)
524 of the map. The second method uses interpolation on the irregular inverse grid
525 with a polynomial.

526 The **Discrete Reconstruction** uses the map; instead of reconstructing the ex-
527 act position of each electron, we reconstruct the center of each hit pad together
528 with the time corresponding to the midpoint of the time bin. The electron count
529 in each TPC bin (consisting of the pad and the time bin) serves as an idealized
530 collected charge, which is then used as a weight in the energy reconstruction fit.

531 3.1 Reconstruction Assuming Steady Drift

532 As the first step, we tried to reconstruct an electron track considering a special
533 set of initial parameters. The origin ([starting point?](#)) of the particle is given by
534 the origin of our coordinate system and its initial direction is given by the pos-
535 itive x -axis. This means the magnetic field of our detector is perpendicular to
536 the momentum of the particle at all times, and we can reduce the problem to
537 two-dimensional space. As an example, we use a track simulated using the mi-
538 croscopic simulation with the kinetic energy 8 MeV. The gas composition used
539 in this simulation is 90:10 Ar:CO₂. [Might be better to describe this track in](#)
540 [Section 2.1 and reference it here.](#)

541 For the reconstruction, we decided to use the common method used in a stan-
542 dard TPC ([similar to?](#)). This will allow us to explore the significance of the atyp-
543 ical behavior in our OFTPC. Additionally, we assume the readout is continuous
544 to further simplify the problem. In this approximation, we reconstruct the initial
545 position of each ionization electron.

546 The reconstruction is then defined by the following relations between the co-
547 ordinates of the detector space and the readout space (see Section 1.3.2): ([some](#)

548 figure, maybe already relating to some track so that it's not too dull)

$$x = x', \quad (3.1)$$

$$y = y', \quad (3.2)$$

$$z = v_d t, \quad (3.3)$$

549 where v_d is the drift velocity of electrons in the given gas mixture. At a phe-
550 nomenological level, this velocity can be considered as a function of the electric
551 field \mathbf{E} and the magnetic field \mathbf{B} as shown in Equation 1.1. **The Garfield++**
552 **toolkit uses this fact to accelerate their drift simulation with non-microscopic**
553 **approaches (could mention in the simulation chapter).** Since we assume a uni-
554 form electric field in the detector and in this approximation we want to neglect
555 the effect of our unusual magnetic field, we consider the drift velocity constant.
556 **Rewrite this while making figures:** We then approximate this velocity by
557 fitting the dependence $z(t)$ taken from the simulated ionization electrons. This
558 is in one of the provisional figures. Also, this description is not completely ac-
559 curate; in reality, we fit $t1:8-y0$ with $a1*x+a0$ and then invert this and use $8-y0$
560 $= b1*t1+b0$ (old coordinates); $b1=1/a1$ functions as the drift velocity. Maybe
561 also define this $8-z$ variable as an alternative to z in Section 1.3.2 and then use it
562 when correcting this.

563 Later, in a commit after this, I plotted some residues (provisional figure),
564 which could be useful, but for some reason they are residuals from a spline fit of
565 the track?! Probably redo this without the spline fit; just explore the difference
566 in individual points.

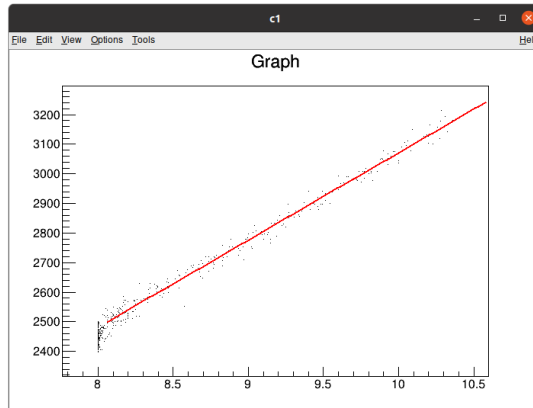


Figure 3.1: Dependence of the drift time on the z coordinate in 90 % argon and 10 % CO_2 atmosphere, fitted with a linear function. The fitted function gives us the average drift velocity in the gas and can be used for rough reconstruction in our TPC. Swap for better image with axis labels, etc. Maybe write the fitted equation.

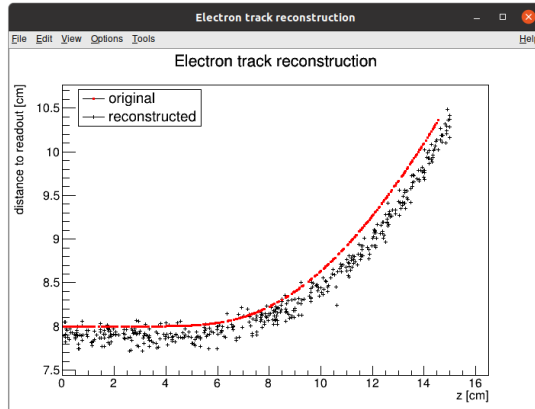


Figure 3.2: The first attempt of a track reconstruction using only the drift velocity. This approach works well in a standard TPC (ideally cite some source). 90 % argon and 10 % CO₂ atmosphere. Swap for better image, correct coordinates.

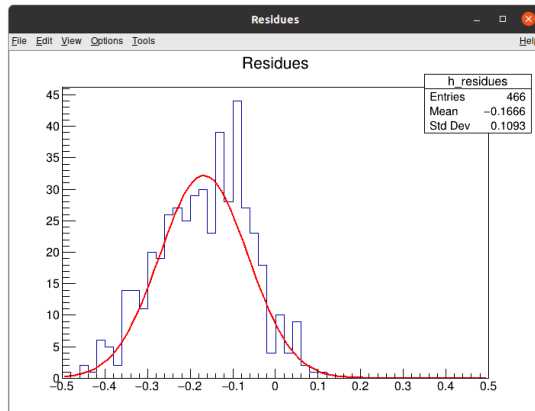


Figure 3.3: First attempt at a track reconstruction using only the drift velocity, residues. Swap for better image, correct coordinates. What's causing the shift? Explain details.

567 3.2 Ionization Electron Map

568 Inside an OFTPC (\exists more than one, also considering it a general concept rather
 569 than the specific OFTPC used at this experiment), the drift of the secondary
 570 (ionization) electrons is significantly affected by its magnetic field (pictures of
 571 the distortion later, the effect is bigger for the 90/10 composition.). We need to
 572 take this into account for accurate reconstruction (should be easy to run the re-
 573 construction without the map and show how much it improves the results). In
 574 the first approximation, we assume a continuous readout (i.e., we neglect the an-
 575 ode segmentation into pads). We can then reconstruct the original position of
 576 each ionization electron using its readout coordinates. For this purpose, we use
 577 the ionization electron map.

578 The ionization electron map represents a mapping from the detector space
 579 to the readout space (see Section 1.3.2). It tells us what readout coordinates

580 (x', y', t) we can expect on average for an ionization electron created at the de-
 581 tector coordinates (x, y, z) . More precisely, it is a mapping to the distributions
 582 on the readout space; we can simplify this as only the means $\bar{\mathcal{M}}$ (**inconsistent**
 583 **notation in the text, write the bar everywhere or nowhere**) and the covariance
 584 matrices \mathcal{M}_{cov} , assuming Gaussian distribution (**test this – some chisq or other**
 585 **statistical test**).

$$\bar{\mathcal{M}} : \mathcal{D} \longrightarrow \mathcal{R}, (x, y, z) \longmapsto (\bar{x}', \bar{y}', \bar{t}). \quad (3.4)$$

586 To get an approximation of this mapping, we simulate the drift of ionization
 587 electrons generated on a regular grid inside the volume of our OFTPC¹. In
 588 order to get accurate results, we use the microscopic simulation of these electrons
 589 described in Section 2.1 (**Monte Carlo from AvalancheMC was also considered**
 590 **but it doesn't (didn't?) include magnetic field, we can probably improve this**
 591 **anyway using the fast track simulation with map proposed in the future section**).
 592 It is also useful to simulate multiple (100 in our case, **this should really only be in**
 593 **a table since there are two map simulations**) electrons originating from the same
 594 position so that we can account for the random fluctuations due to collisions.

595 When evaluating the map inside the grid, we use trilinear interpolation (see
 596 Section 1.3.3). From now on, we will use the same symbol \mathcal{M} for this interpolated
 597 simulation.

598 Finally, we need to invert the map to get the original detector coordinates
 599 (x, y, z) from the given readout coordinates (x', y', t) . In our case, it is reasonable
 600 to assume that the mapping $\bar{\mathcal{M}}$ (**of means (notation inconsistency)**, we lose the
 601 **information about the distribution** (a wild idea how to recover this is in the Future
 602 **section but it will only make sense if the GEM is already accounted for and is**
 603 **very preliminary as there are many factors to consider**) is one-to-one (as seen in
 604 the simulations). We implemented two methods for this purpose: the gradient
 605 descent search (Section 3.2.1) and interpolation on the inverse grid (Section 3.2.2).

606 The simulation (?) of the map is a computationally heavy task. For this rea-
 607 son, we use the MetaCentrum grid [3] to parallelize needed calculations. At first,
 608 this was done by evenly distributing the simulated electrons across the individual
 609 jobs in a simulation with only one electron per vertex in the regular grid with
 610 a spacing of one centimeter. Later, a more efficient approach was implemented,
 611 accounting for the varying lengths of the drift of individual electrons. If we in-
 612 dex the electrons in the order of increasing coordinates y, x, z (**picture will make**
 613 **things clearer**), we can express the number n_l of full XY layers (i.e., electrons
 614 with the same z coordinate) of electrons with index less than or equal to i

$$n_l(i) = \left\lfloor \frac{i}{n_{xy}} \right\rfloor, \quad (3.5)$$

615 where n_{xy} is the number of electrons in each XY layer calculated simply by count-
 616 ing the electrons that satisfy boundary conditions for x and y . **These conditions**
 617 **should be mentioned above; sector condition + maximal x value.** The number of
 618 electrons remaining in the top layer is then

$$n_r(i) = i \bmod n_{xy}. \quad (3.6)$$

¹The detector walls are not considered and we simulate the drift even outside of the OFTPC which allows us to interpolate even close to the walls

619 Finally, we can calculate the sum of the drift gaps of electrons up to index i

$$d_{\text{sum}} = (z_{\max} - z_{\min})n_{xy}n_l - \frac{n_l(n_l - 1)}{2}n_{xy}l + n_r(z_{\max} - z_{\min} - n_l l). \quad (3.7)$$

620 We then use a binary search algorithm to find the maximum index i such that
621 the value of this sum is less than the fraction $\frac{\text{job id}}{\max \text{ job id}}$ of the total sum. This way
622 we obtain the minimal and the maximal index of electrons simulated in the given
623 job. The spacing l should be probably defined above + picture of the simulating
624 grid (1 layer). zmin zmax also

625 After the simulation of the map, we calculate the mean readout coordinates
626 assuming Gaussian distribution (i.e., we use averages). We also calculate standard
627 deviations in a later commit, should be upgraded to the covariance matrix. We
628 never actually plotted the distributions we get when simulating the same electron
629 multiple times, so we do not know if our assumptions are accurate (could also
630 run some statistical test to see how well the Gaussian distribution fits).

631 The obtained map is then stored in a custom class template *Field*, could
632 expand on that. Maybe earlier, since the same template is used for the magnetic
633 field.

634 Could insert a table here describing all 4 simulations of the map (gas composi-
635 tion, spacing, etc.). Simulation inside of one sector (at first double angle). Extra
636 space on the sensor. Edge cases not taken into account (TPC wall). Using qsub
637 (not sure if important). Add plots of distortion of the coordinates. Could also do
638 these plots in a different way (e.g., drawing all the endpoints of each ionization
639 electron or some error ellipse plot).

640

641 Images to add (comparison of both simulations):

- 642 • 3D visualization of the map, simulation example
- 643 • z vs. t plot
- 644 • XY plane distortion for different z values; with arrows and error bars, for
645 all z -layers with different colors
- 646 • XZ plane ($y = 0$) distortion in x (maybe not necessary?)
- 647 • XT plot ($y = 0$) showing (small) distortion in drift times

648

649 More images:

- 650 • Residuals of the continuous readout reconstruction.

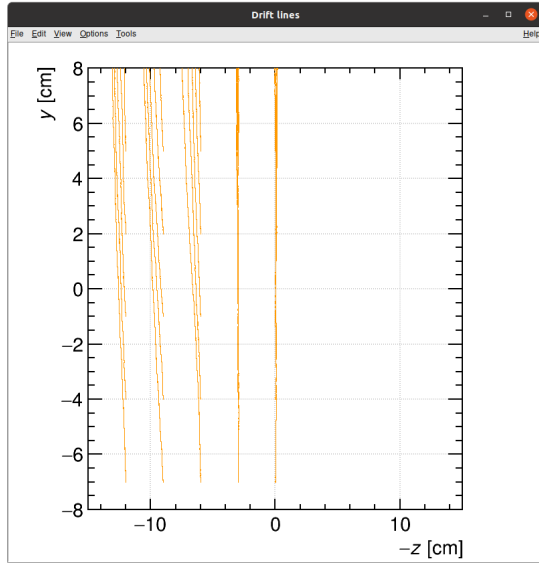


Figure 3.4: Example of map generation. Swap for better image, correct coordinates.

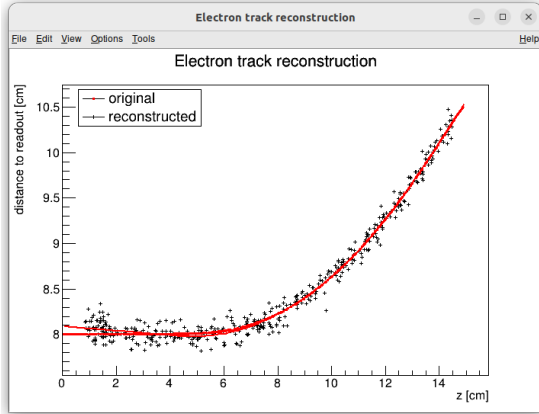


Figure 3.5: Example reconstruction with the map. Swap for better image, correct coordinates.

651 3.2.1 Gradient Descent Algorithm

652 The first implemented method of reconstruction uses a gradient descent algorithm
 653 to calculate an inversion of the map $\bar{\mathcal{M}}$ in a given point. Gradient descent is
 654 an iterative minimization algorithm for multivariate functions. Let $R \in \mathcal{R}$ be
 655 a point in the readout space; we want to find a point $D = (x, y, z) \in \mathcal{D}$ in
 656 the detector space such that

$$\bar{\mathcal{M}}(D) = R = (x'_R, y'_R, t_R). \quad (3.8)$$

657 We define a function f_R in the readout space as a distance in this space:

$$f_R(x', y', t) = \sqrt{(x' - x'_R)^2 + (y' - y'_R)^2 + v_d^2(t - t_R)^2}, \quad (3.9)$$

658 where v_d is an approximation of the drift velocity in the TPC, obtained from
 659 the reconstruction in Section 3.1 (there will be an image with the linear fit here).

660 We make an initial guess (actually in the original code we just take $z = 0$):

$$D_0 = (x'_R, y'_R, v_d t). \quad (3.10)$$

661 Assuming we have the n -th estimate D_n , we calculate the i -th component of
662 the gradient of $f_R \circ \bar{\mathcal{M}}$ numerically using central differences: (signs look correct)

$$[\nabla(f_R \circ \bar{\mathcal{M}})]^i(D_n) \approx \frac{f_R(\bar{\mathcal{M}}(D_n + s \cdot e^i)) - f_R(\bar{\mathcal{M}}(D_n - s \cdot e^i))}{2s}, \quad (3.11)$$

663 where $e^i \in \mathcal{D}$ is the i -th coordinate vector and s is the step size. The step size
664 should be sufficiently small; initially, we set it as a fraction $s = \frac{l}{10}$ of the map's
665 grid spacing l . During the minimization, we check that $f_R(\bar{\mathcal{M}}(D_n)) < 10s$ at all
666 times (s can (?) change – check). When using trilinear interpolation, it would be
667 more efficient to calculate the gradient explicitly (\pm same result). This could be
668 implemented inside the *Field* template class. The next iteration can be calculated
669 as follows:

$$D_{n+1} = D_n - \gamma \nabla(f_R \circ \bar{\mathcal{M}})(D_n), \quad (3.12)$$

670 where $\gamma \in \mathbb{R}^+$ is the damping coefficient. It should be set to a small enough
671 value to ensure convergence, but large enough for sufficient converging speed.
672 The minimization stops either when the error $f_R(\bar{\mathcal{M}}(D_n))$ drops below a specified
673 value or when the number of iterations exceeds a certain limit (in this case,
674 a message is printed into the console). The parameters of this method can be
675 further optimized (e.g., a better choice of γ , gradient computation); instead, we
676 later decided to use the interpolation on the inverse grid described in the next
677 section.

678 Measure reconstruction duration and compare it with the inverse grid inter-
679 polation? Also compare the result? Typical evolution of D_n during search. Not
680 sure if this has to be cited.

681 3.2.2 Interpolation on the Inverse Grid

682 Interpolation should be generally faster than the gradient descent since we don't
683 need to iterate. We also don't need to optimize it to improve performance, if
684 it's too slow we can even calculate the coefficients for the entire map before
685 reconstruction (again, do some profiling).

686 The best current algorithm uses the interpolation on the inverse grid. Rather
687 than inverting the trilinearly interpolated map using a numerical minimization
688 method as in the previous section, we take advantage of the fact that the map
689 $\bar{\mathcal{M}}$ is one-to-one (isomorphism is supposed to preserve structure, not sure how
690 to interpret that here, not the best description, we already (kind of) assume it
691 is a bijection by saying we will invert it). Since we have simulated values of this
692 map on a regular grid in the detector space \mathcal{D} , we also know the inverse map $\bar{\mathcal{M}}^{-1}$
693 on the irregular inverse grid in the readout space \mathcal{R} . To get an approximation
694 of the inverse map in the entire readout space, we can use interpolation (general
695 concept, the specific choice is described below).

696 Since the inverse grid is irregular, trilinear interpolation cannot be applied.
697 Given that the simulated map is dense enough to provide a good approximation

698 considering the size of our pads, we can adopt a similar approach.² As shown in
 699 Equation 1.20 in Section 1.3.3, trilinear interpolation (**shouldn't need an article**
 700 **when talking about a general concept**) can be expressed as a polynomial:

$$\hat{f}(x, y, z) = axyz + bxy + cxz + dyz + ex + fy + gz + h, \quad (3.13)$$

701 where a, b, c, d, e, f, g, h are coefficients uniquely determined by the values of
 702 the function at the vertices of the interpolation cell (**can be calculated in the**
 703 **way shown in the mentioned equation, not sure what more to add**). We can gen-
 704 eralize this for a function defined on an irregular grid. Given the function values
 705 at any eight points, we can write a system of eight linear equations

$$\begin{pmatrix} x_1y_1z_1 & x_1y_1 & x_1z_1 & y_1z_1 & x_1 & y_1 & z_1 & 1 \\ \vdots & \vdots \\ x_8y_8z_8 & x_8y_8 & x_8z_8 & y_8z_8 & x_8 & y_8 & z_8 & 1 \end{pmatrix} \begin{pmatrix} a \\ \vdots \\ h \end{pmatrix} = \begin{pmatrix} f(x_1, y_1, z_1) \\ \vdots \\ f(x_8, y_8, z_8) \end{pmatrix}, \quad (3.14)$$

706 which has a unique solution for the coefficients for most values of (x_n, y_n, z_n) and
 707 $f(x_n, y_n, z_n)$, where $n \in \{1, \dots, 8\}$.

708 This approach introduces a small complication: finding the correct pseudocell
 709 (i.e., the image of eight vertices forming a cubic cell in the regular grid) in
 710 the inverse grid. The eight irregularly spaced vertices of this pseudocell do not
 711 define a unique volume, so there are multiple possible ways to partition \mathcal{R} into
 712 pseudocells, with no obvious choice among them.

713 We are currently ignoring this problem and performing binary search along
 714 x, y, z (in this order). It shouldn't matter too much because the 70/30 map
 715 doesn't cause such a big distortion and was even accidentally extrapolated for all
 716 z different from the central plane.

²A more complicated and computationally heavy alternative would be natural neighbor interpolation or Kriging.

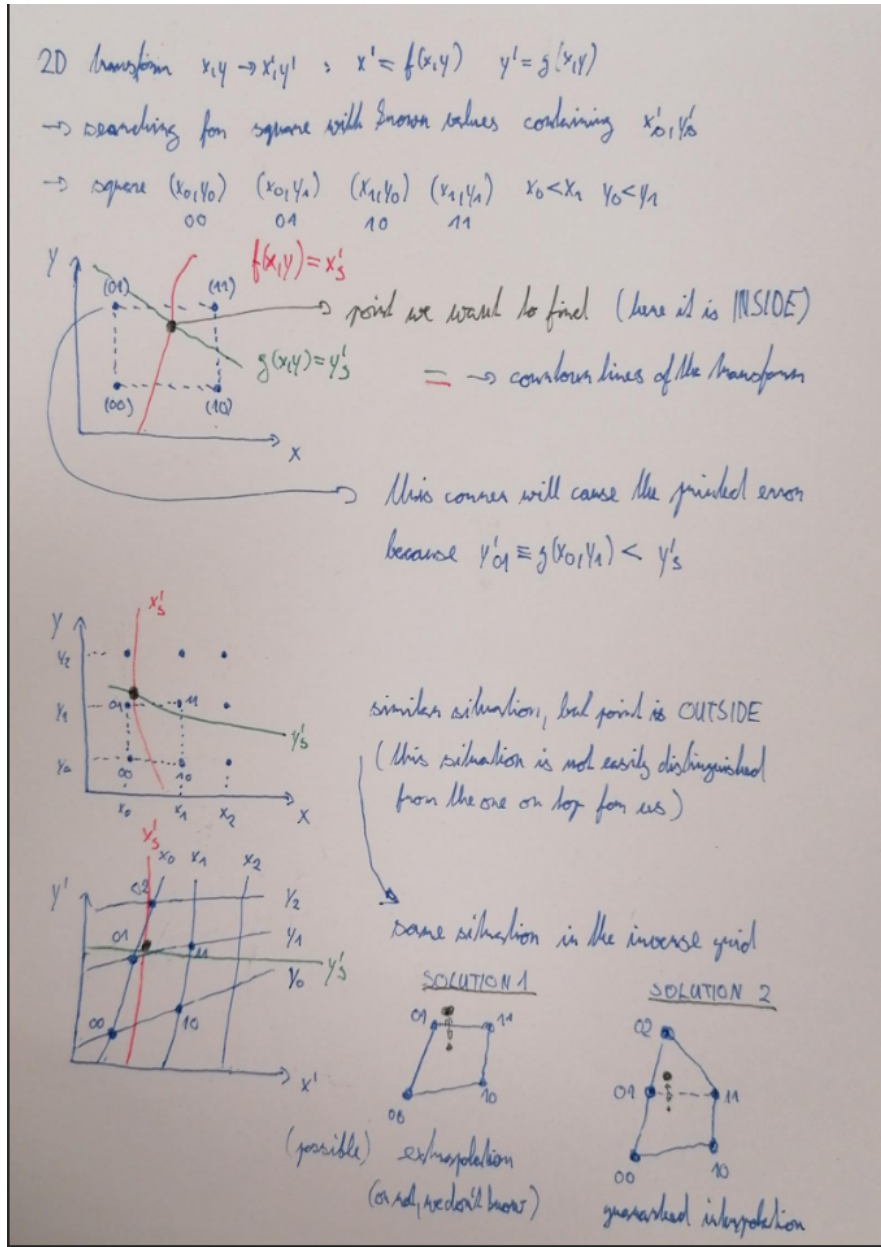


Figure 3.6: Selection of the points for interpolation. Create better images; use the explanation interpolation vs. extrapolation strange property. Solution 2 probably does not make much sense.

717 3.3 Discrete Reconstruction

718 Reconstruction with pads and time bins. Maybe testing different pads.

719 It is also possible to make this a subsection of the map, making the previous
720 subsections parts of a new subsection 'Map Inversion'.

721 In order to get a more realistic representation of a track measured in the OFTPC,
722 we need to take the discretization of the position and time data into account.
723 The readout of the OFTPC will consist of 128 pads, their layout is shown in
724 Figure 1.6. Time is read out in discrete bins of size $t_{\text{bin}} = 100$ ns.

725 As the first approximation, we can neglect the multiplication in the triple-GEM.

726 and assume an ideal charge readout. The time measurement starts at the begin-
 727 ning of the electron/positron simulation (depending on the specific simulation it
 728 can correspond to the production in the target or when entering the OFTPC,
 729 here the specific time doesn't matter too much since the primary particle trav-
 730 els basically at light speed (30 ps/cm) which is circa immediate given the time
 731 binning). Randomize this time a bit and see what it does to the reconstruction.
 732 The readout coordinates $(x', y', t) \in \mathcal{R}$ of each ionization electron can be mapped
 733 to the pad coordinates $(n_{\text{pad}}, n_t) \in \mathcal{P}$:

$$n_{\text{pad}} = n: (x', y') \in \left[x_{1,n} - \frac{g}{2}, x_{2,n} + \frac{g}{2} \right] \times \left[y_{1,n} - \frac{g}{2}, y_{2,n} + \frac{g}{2} \right], \quad (3.15)$$

$$n_t = \left\lceil \frac{t}{t_{\text{bin}}} \right\rceil, \quad (3.16)$$

734 where $x, y_{1,n}$ and $x, y_{2,n}$ are the opposing pad corner coordinates, and g is the
 735 gap between the pads (described in detail in Section 1.3.2). This way, the closest
 736 pad is assigned to each readout position within the OFTPC volume³. Makes
 737 sense since the pads attract the electrons, the inhomogeneity of electric field is
 738 neglected. The number of electrons collected by each pad (i.e., collected charge)
 739 in each time bin is then counted and serves as a weight for the energy recon-
 740 struction. The reconstructed track consists of points for each $(n, n_t) \in \mathcal{P}$, we get
 741 these by reconstructing the position of a hypothetical electron with the readout
 742 coordinates of the pad/time bin center:⁴

$$\mathcal{D} \ni (x, y, z) = \overline{\mathcal{M}} \left(x_{c,n}, y_{c,n}, \left(n_t - \frac{1}{2} \right) t_{\text{bin}} \right). \quad (3.17)$$

³Some positions near the wall are not handled and some pads extend beyond the OFTPC volume. This is where an electric field simulation would come in handy.

⁴Mapping the center of the pad (along with the midpoint of the time bin) isn't necessarily the best approach since it might not correspond to the average parameters of an electron with these readout parameters.

743 4. Energy Reconstruction

744 The second stage is the reconstruction of the particle's energy using a fit of its
745 reconstructed track (see Section 3). We have tested three ways of reconstructing
746 the energy. Fitting is done using the MINUIT algorithm implemented in
747 ROOT [2]. Cite some CERN article directly on MINUIT, can add a section. Or
748 is it done using MIGRAD? The circle and RK4 probably was.

749 The **Cubic Spline Fit** was a tested and later rejected method of energy reconstruction.
750 It uses smoothly connected piecewise cubic polynomials between uniformly spaced nodes.
751 The reconstructed energy is calculated using the fit parameters by computing the radius of curvature in different points of the fitted
752 curve using the known magnitude of the magnetic field perpendicular to the trajectory.
753 We rejected this method because the tuning of the fit turned out to be unpractical compared to the other used methods.
754 Reconstructs energy at every position (even though the actual energy doesn't change much) and it might be
755 slower but no profiling has been done yet. Of course, it wasn't tested on the
756 newer track reconstruction methods at all.

757 The **Circle and Lines Fit** was chosen as an alternative since this corresponds to the shape of a trajectory of a charged particle crossing a finite volume
758 with a homogeneous magnetic field. The energy of the particle can be estimated
759 using the fitted radius and the magnitude of the perpendicular magnetic field in
760 the middle of the TPC.

761 The **Runge-Kutta Fit** uses the 4th order Runge-Kutta numerical integration
762 described in Section 2.2. Initial parameters of the track (including the particle's
763 energy) are optimized so that the integrated trajectory fits to the reconstructed
764 one. This fit can also be performed as a single parameter (i.e., energy) fit if we
765 get the initial position and orientation of the particle on the entrance to the TPC
766 from previous detectors (**Tpx3!** (**Tpx3!**) and MWPC, see Section 0.2).

770 4.1 Cubic Spline Fit

771 The first attempt to get an estimate of the kinetic energy of the particle uses
772 a cubic spline fit. We use an electron track starting in the origin of our coordinate

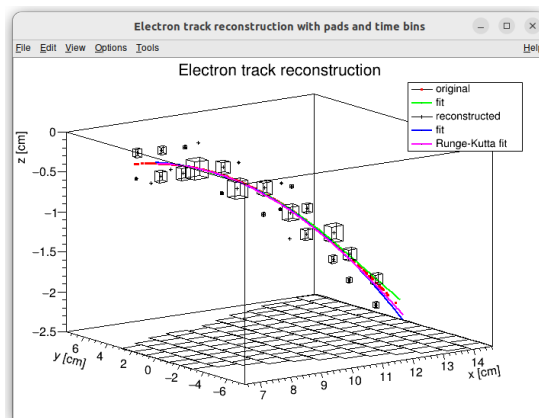


Figure 4.1: Example of a fitted reconstructed track. Swap for better image.

773 system with an initial direction in the positive x axis. The example track is
 774 simulated microscopically (see Section 2.1) with a kinetic energy of 8 MeV in
 775 a gas mixture 90% Ar + 10% CO₂ (the same track was used in Section 3.1). **This**
 776 **track should probably be described in the simulation chapter.**

777 In order to calculate the spline, we use the class *TSplines3* from ROOT. This
 778 allows us to evaluate the spline using the coordinates (x_n, z_n) of each node and
 779 the derivatives d_1, d_2 in the first and the last node. We can fit these parameters
 780 of a fixed amount of nodes to the simulated trajectory. We use the IMPROVE
 781 algorithm provided by the *TMinuit* class in ROOT (**there are some guidelines for**
 782 **fonts in MFF UK template (Czech version) that I will eventually apply (see notes**
 783 **in the conclusion)**). This algorithm attempts to find a better local minimum after
 784 converging (**could reformulate a bit, taken word for word from some manual**).

785 After the fit converges, we calculate an energy estimate using the radius of
 786 curvature, which we can extract from the fitted spline equation at every point of
 787 the trajectory. The part of the spline corresponding to a given node is defined as

$$z(x) = z_n + b\Delta x + c(\Delta x)^2 + d(\Delta x)^3, \quad (4.1)$$

788 where $\Delta x = x - x_n$ and b, c, d are coefficients. Using this equation, we derive
 789 the radius of curvature¹ as:

$$r(x) = \frac{(1 + z'^2(x))^{\frac{3}{2}}}{z''(x)} = \frac{(1 + (b + 2c\Delta x + 3d(\Delta x)^2)^2)^{\frac{3}{2}}}{2c + 6d\Delta x}. \quad (4.2)$$

790 Based on the geometry of our detector, we assume that the magnetic field satisfies
 791 $\mathbf{B}(x, 0, z) = (0, B(x, z), 0)$ for a track in the XZ plane. Since the electron is rela-
 792 tivistic, the effect of the electric field on its trajectory is negligible. The Lorentz
 793 force F_L is then always perpendicular to the momentum of the electron and acts
 794 as a centripetal force F_c (**not quite sure how to handle this then?**):

$$\begin{aligned} \mathbf{F}_L &= \mathbf{F}_c, \\ \|e\mathbf{v} \times \mathbf{B}\| &= \frac{\gamma m_e v^2}{r}, \\ ec\beta B &= \frac{E_{0e}\beta^2}{r\sqrt{1 - \beta^2}}, \end{aligned} \quad (4.3)$$

$$\begin{aligned} \sqrt{1 - \beta^2} &= \frac{E_{0e}\beta}{ecBr}, \\ \beta^2(x) &= \left[1 + \left(\frac{E_{0e}}{ecB(x, z(x))r(x)}\right)^2\right]^{-1}, \end{aligned} \quad (4.4)$$

795 where e is the elementary charge, c is the speed of light in vacuum, m_e is the rest
 796 mass of electron, $E_{0e} = m_e c^2$ is its rest energy, γ is the Lorentz factor, \mathbf{v} is
 797 the velocity of the electron, and $\beta = \frac{v}{c}$. The kinetic energy for a given point on
 798 the trajectory is then given as

$$E_{\text{kin}}(x) = \left(\frac{1}{\sqrt{1 - \beta^2(x)}} - 1\right) E_{0e}. \quad (4.5)$$

¹For the general formula see https://en.wikipedia.org/wiki/Curvature#Graph_of_a_function.

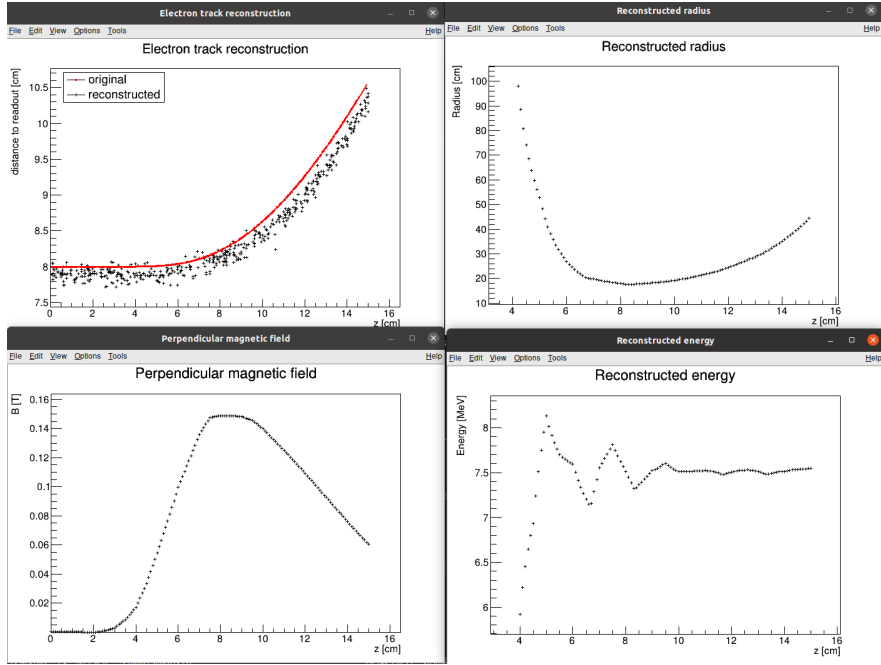


Figure 4.2: First attempt at a track reconstruction using only the drift velocity. Spline energy reconstruction attempt. Swap for better image(s) – subfigure environment, correct coordinates.

799 We can then average these estimates at multiple points (possibly using some
800 weights to account for the change in accuracy, this wasn't optimized and we just
801 ended with the graph) to get a single value. This method was later rejected in
802 favor of the circle and lines fit the name was already established at the beginning
803 of the chapter described in the next section. Add some figures.

804 4.2 Circle and Lines Fit

805 Another way to estimate the particle's kinetic energy is to fit its (??) trajectory
806 with a circular arc with lines attached smoothly. This shape of trajectory cor-
807 responds to a movement of a charged particle through a homogeneous magnetic
808 field perpendicular to the particle's momentum and limited to a certain volume.
809 In general, the shape of such a trajectory with a non-perpendicularly oriented
810 momentum is a spiral. In our case, the magnetic field is approximately toroidal
811 and the particle motion is nearly perpendicular to it (verify, could add some
812 magnetic field plots in different vertical planes; shouldn't have a big effect on the
813 reconstructed radius anyway). At first, we tested a 2D version of this fit, then
814 we adapted it to 3D.

815 The field in our detector is not homogeneous, it is therefore not entirely clear
816 what value of magnetic field should be used along with the fitted radius (using
817 equations 4.4 and 4.5) to get the best estimate for the kinetic energy. Since we
818 only use this method as the first iteration of the particle's energy that we later
819 refine, an optimal solution of this problem is not required. Instead, we tested two
820 options: taking the value of the field in the middle of the fitted circular arc (or
821 is it in the middle x of the OFTPC?) and taking the average field along it. We

haven't really tried to plot this for multiple tracks, but these estimates are saved somewhere and could be plotted.

4.2.1 Two-dimensional fit

In the 2D case, the fitted function used for the electron track² described in Section 4.1 (or in microsim? one specific track at the time, technically this function doesn't work for a curvature that gets outside of the semicircle) is defined as follows: Maybe describe this track that we used at the beginning somewhere earlier (section microscopic simulations → Testing track?) so that it is easier to refer to it in multiple sections. It is not part of the early GitHub commits, so maybe it won't be possible to create exact replicas of the images, but they should be at least very similar.

$$z(x) = \begin{cases} a_1x + b_1 & x < x_1 \\ z_0 + \sqrt{r^2 - (x - x_0)^2} & x_1 \leq x \leq x_2 \\ a_2x + b_2 & x > x_2 \end{cases}, \quad (4.6)$$

where $a_{1,2}$ and $b_{1,2}$ are the parameters of the lines, (x_0, z_0) is the center of the circle, r is its radius, and $(x_{1,2}, z_{1,2})$ are the coordinates of the function's nodes. That means we have 9 parameters ($z_{1,2}$ are not used in the function) along with 2 continuity conditions and 2 smoothness conditions (9 parameters of the described function, 5 of them independent after taking the conditions into account). For the fit, we use the coordinates of the nodes and the radius of the circle, which gives us 5 independent parameters (only the radius has to be larger than half of the distance between nodes). The continuity conditions (combined with the relations for $z_{1,2}$) are

$$z_{1,2} = a_{1,2}x_{1,2} + b_{1,2} = z_0 - \sqrt{r^2 - (x_{1,2} - x_0)^2}, \quad (4.7)$$

the smoothness conditions are

$$a_{1,2} = \frac{x_0 - x_{1,2}}{\sqrt{r^2 - (x_{1,2} - x_0)^2}}. \quad (4.8)$$

Together with the Equation 4.7 we get the values of $b_{1,2}$

$$b_{1,2} = z_{1,2} - a_{1,2}x_{1,2}. \quad (4.9)$$

For the coordinates of the center of the circle, we can use the fact that the center has to lie on the axis of its chord. In other words, there is a value of a parameter t such that, using the parametric equation of the axis

$$\begin{pmatrix} x_0 \\ z_0 \end{pmatrix} = \begin{pmatrix} \frac{x_1+x_2}{2} \\ \frac{z_1+z_2}{2} \end{pmatrix} + t \begin{pmatrix} \frac{z_2-z_1}{2} \\ \frac{x_1-x_2}{2} \end{pmatrix}. \quad (4.10)$$

At the same time, the center has to be in a distance of r from the nodes:

$$\begin{aligned} (x_1 - x_0)^2 + (z_1 - z_0)^2 &= r^2, \\ \left(\frac{x_1 - x_2}{2} + \frac{z_1 - z_2}{2}t \right)^2 + \left(\frac{z_1 - z_2}{2} + \frac{x_2 - x_1}{2}t \right)^2 &= r^2, \\ \left(\left(\frac{x_2 - x_1}{2} \right)^2 + \left(\frac{z_2 - z_1}{2} \right)^2 \right)t^2 + \left(\frac{x_2 - x_1}{2} \right)^2 + \left(\frac{z_2 - z_1}{2} \right)^2 - r^2 &= 0. \end{aligned} \quad (4.11)$$

²Electron tracks bend towards negative z , we need to use the upper part of the circle

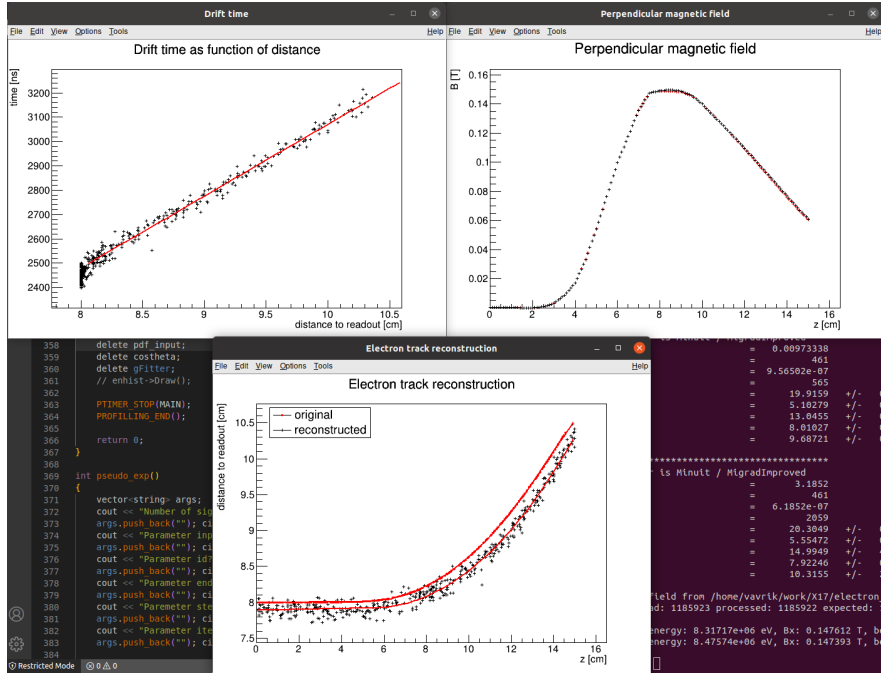


Figure 4.3: First attempt at a track reconstruction using only the drift velocity. Circle and Lines Fit in 2D. Swap for better image, correct coordinates. Bias should be described in the previous chapter, not here.

848 Since our electron track bends towards negative z and $x_2 > x_1$, we only care
849 about the solution with $t > 0$

$$t = \sqrt{\frac{r^2}{\left(\frac{x_2-x_1}{2}\right)^2 + \left(\frac{z_2-z_1}{2}\right)^2} - 1}, \quad (4.12)$$

$$\begin{aligned} x_0 &= \frac{x_1 + x_2}{2} + \frac{z_2 - z_1}{2} \sqrt{\frac{r^2}{\left(\frac{x_2-x_1}{2}\right)^2 + \left(\frac{z_2-z_1}{2}\right)^2} - 1}, \\ z_0 &= \frac{z_1 + z_2}{2} - \frac{x_2 - x_1}{2} \sqrt{\frac{r^2}{\left(\frac{x_2-x_1}{2}\right)^2 + \left(\frac{z_2-z_1}{2}\right)^2} - 1}. \end{aligned} \quad (4.13)$$

850 The function defined in Equation 4.6 along with equations 4.8, 4.9, and 4.13
851 derived using the continuity and smoothness conditions (combined with the re-
852 lations for $z_{1,2}$) fully define our fitted function with parameters $r, x_{1,2}, z_{1,2}$. Some
853 pictures of the fit on the tested track. Results of the fit. Again, the actual fit
854 uses 8-z. Use GeoGebra schematics to generate a picture of 2D geometry.

855 4.2.2 Three-dimensional fit

856 Explain the geometry and least square method used for the 3D fit. Tested on
857 a Runge-Kutta sample, and with microscopic tracks + map simulation.

858 In three dimensions, the shape of a trajectory of a charged particle in a uniform
859 magnetic field is a cylindrical helix. Nevertheless, since we assume that the
860 field is approximately perpendicular to the particle's momentum at all times, we

will further approximate the trajectory with a circular arc (with lines attached smoothly).

We assume that the initial position $\mathbf{X}_0 = (x_0, y_0, z_0)$ and direction θ, φ (spherical angles as in Section 1.3.2) are known, since this information will be provided by **Tpx3!** and MWPC layers. We could further refine it at the end of the current algorithm with some kind of global fit (all detector layers). The fit then has four free parameters (figure):

- the length of the first line l (as measured from the initial position),
- the radius of the circular arc r ,
- the central angle of the arc $\phi_{\max} \in [0, 2\pi]$,
- the direction of the curvature given by the angle $\alpha \in [0, 2\pi]$ (right-handed with respect to the particle direction, $\alpha = 0$ if the particle curves towards negative z in a plane given by $\hat{\mathbf{z}}$ and the direction vector).

Using these parameters, we can derive a parametrization of the whole curve. Let \mathbf{v} be the initial unit direction vector, i.e., using the spherical angles

$$\mathbf{v} = (\cos \varphi \cos \theta, \sin \varphi \cos \theta, \sin \theta)^T, \quad (4.14)$$

then we can parameterize the first line as follows:

$$\mathbf{X}_{L1}(t) = \mathbf{X}_0 + t\mathbf{v} \quad t \in [0, l]. \quad (4.15)$$

This gives us the starting point of the arc

$$\mathbf{X}_1 = \mathbf{X}_{L1}(l) = \mathbf{X}_0 + l\mathbf{v}. \quad (4.16)$$

The vector \mathbf{c}_1 that lies in the plane of curvature and points from \mathbf{X}_1 to the center of curvature can be calculated using a composition of rotations. First, we rotate \mathbf{v} to point in the $\hat{\mathbf{x}}$ direction, the normal for $\alpha = 0$ than points in the $-\hat{\mathbf{z}}$ direction, we apply the α rotation and reverse the rotations into the $\hat{\mathbf{x}}$ direction: (parameters are explained in the bullet points above)

$$\begin{aligned} \mathbf{c}_1 &= R_z(\varphi)R_y(-\theta)R_x(\alpha)R_y\left(\frac{\pi}{2}\right)R_y(\theta)R_z(-\varphi)\mathbf{v}, \\ &= R_z(\varphi)R_y(-\theta)R_x(\alpha)(-\hat{\mathbf{z}}), \\ &= \begin{pmatrix} \cos \varphi & -\sin \varphi & 0 \\ \sin \varphi & \cos \varphi & 0 \\ 0 & 0 & 1 \end{pmatrix} \begin{pmatrix} \cos \theta & 0 & -\sin \theta \\ 0 & 1 & 0 \\ \sin \theta & 0 & \cos \theta \end{pmatrix} \begin{pmatrix} 1 & 0 & 0 \\ 0 & \cos \alpha & -\sin \alpha \\ 0 & \sin \alpha & \cos \alpha \end{pmatrix} \begin{pmatrix} 0 \\ 0 \\ -1 \end{pmatrix}, \quad (4.17) \\ &= \begin{pmatrix} -\sin \alpha \sin \varphi + \cos \alpha \cos \varphi \sin \theta \\ \sin \alpha \cos \varphi + \cos \alpha \sin \varphi \sin \theta \\ -\cos \alpha \cos \theta \end{pmatrix}. \end{aligned}$$

Signs should be correct because right-handed rotation around y rotates z into x and this one is the opposite. Seems like in this part of the code θ is actually taken from the pole. Instead of the equator plane. Similarly by rotating $\hat{\mathbf{y}}$, we can get the normal vector $\mathbf{n} = \mathbf{v} \times \mathbf{c}_1$ perpendicular to the plane of the trajectory:

$$\mathbf{n} = R_z(\varphi)R_y(-\theta)R_x(\alpha)\hat{\mathbf{y}} = \begin{pmatrix} -\cos \alpha \sin \varphi - \sin \alpha \cos \varphi \sin \theta \\ \cos \alpha \cos \varphi - \sin \alpha \sin \varphi \sin \theta \\ \sin \alpha \cos \theta \end{pmatrix}. \quad (4.18)$$

887 This allows us to express the coordinates of the center \mathbf{C} of the circular arc:

$$\mathbf{C} = \mathbf{X}_1 + r\mathbf{c}_1. \quad (4.19)$$

888 We can then get the parametrization and the endpoint of the circular arc using
889 Rodrigues' rotation formula: (all parameters explained in the bullet points above)

$$\begin{aligned} \mathbf{c}_2 &= \mathbf{c}_1 \cos \phi_{\max} + (\mathbf{n} \times \mathbf{c}_1) \sin \phi_{\max} + \mathbf{n}(\mathbf{n} \cdot \mathbf{c}_1)(1 - \cos \phi_{\max}), \\ &= \mathbf{c}_1 \cos \phi_{\max} - \mathbf{v} \sin \phi_{\max}, \end{aligned} \quad (4.20)$$

$$\mathbf{X}_C(\phi) = \mathbf{C} - r(\mathbf{c}_1 \cos \phi - \mathbf{v} \sin \phi) \quad \phi \in [0, \phi_{\max}], \quad (4.21)$$

$$\mathbf{X}_2 = \mathbf{X}_C(\phi_{\max}) = \mathbf{C} - r\mathbf{c}_2, \quad (4.22)$$

890 and if we define the direction vector of the second line, we also get its parametriza-
891 tion

$$\mathbf{w} = \mathbf{v} \cos \phi_{\max} + (\mathbf{n} \times \mathbf{v}) \sin \phi_{\max} = \mathbf{v} \cos \phi_{\max} + \mathbf{c}_1 \sin \phi_{\max}, \quad (4.23)$$

$$\mathbf{X}_{L2}(s) = \mathbf{X}_2 + s\mathbf{w} \quad s \in [0, \infty). \quad (4.24)$$

892 The fit is performed as a (weighted) least square minimization (**MIGRAD**
893 **ROOT**), therefore we need to derive the distance of any point \mathbf{P} to the fitted
894 curve. For the first line, we simply compute the parameter value of the closest
895 point on the line:

$$\begin{aligned} t_P &= \mathbf{v} \cdot (\mathbf{P} - \mathbf{X}_1), \\ d_{P1} &= \|\mathbf{P} - \mathbf{X}_{L1}(t_P)\|. \end{aligned} \quad (4.25)$$

896 If the parameter value is outside of its bounds defined above, we take the bound-
897 ary value instead. The distance to the second line is computed likewise. For
898 the circular arc (specific circular arc in the fit), we find the closest point (on the
899 arc) by projecting the center connecting line onto the arc plane:

$$\mathbf{X}_{PC} = \mathbf{X}_C + r \frac{(\mathbf{P} - \mathbf{X}_C) - (\mathbf{n} \cdot (\mathbf{P} - \mathbf{X}_C))\mathbf{n}}{\|(\mathbf{P} - \mathbf{X}_C) - (\mathbf{n} \cdot (\mathbf{P} - \mathbf{X}_C))\mathbf{n}\|}, \quad (4.26)$$

$$d_{PC} = \|\mathbf{P} - \mathbf{X}_{PC}\| \quad (4.27)$$

900 Potential problem in the implementation – might not be correctly handling ϕ
901 out of bounds, the distance could be sometimes underestimated because of this.

902 The shortest distance out of d_{P1}, d_{PC}, d_{P2} is then taken as the distance to the curve. ■

903 When calculating energy with the average field, only the arc is considered. Mid-
904 dle field in the current implementation taken in the middle x plane (intersection
905 with the curve). TVirtualFitter+MIGRAD, maximal num of iterations, tolera-
906 tion. Different uncertainties in x, y, z not taken into account.

907 4.3 Runge-Kutta Fit

908 The Runge-Kutta fit uses the Runge-Kutta 4th order (RK4) numerical integra-
909 tion of the equation of motion (see Section 2.2) to find the best values of the track
910 parameters – the track origin, initial velocity direction and the kinetic energy. In
911 order to speed up the energy reconstruction, an initial guess of these parameters
912 can be obtained from the 3D circle fit described in the previous section. Fur-
913 thermore, assuming we know the track origin and orientation, we can perform

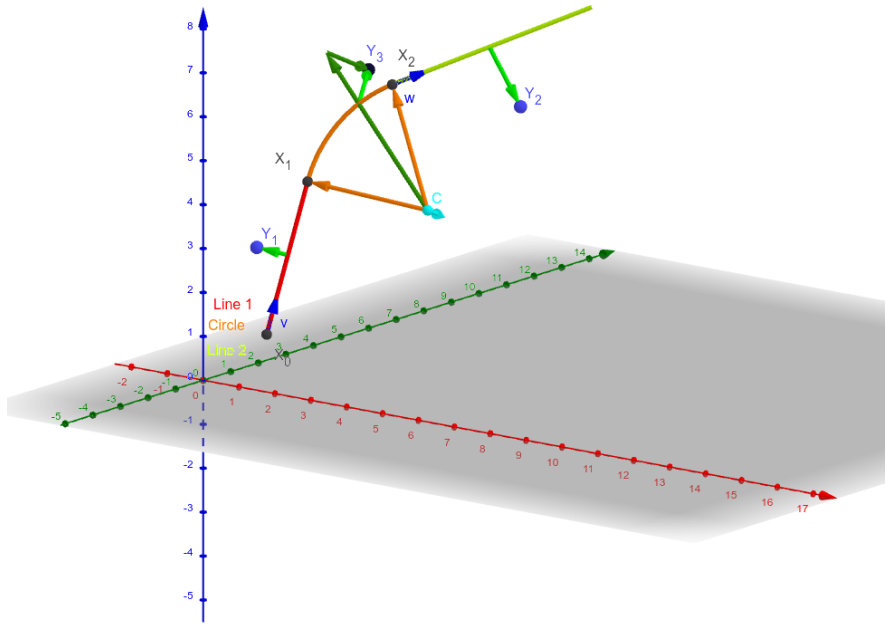


Figure 4.4: Circle and Lines Fit 3D geometry. Swap for better image.

914 a single parameter fit of the kinetic energy (**do some profiling and show that it is**
 915 **faster – below in the microscopic testing**).

916 The fit is performed as a least square minimization of the (weighted) distances
 917 of the track points (true ionization vertices from the simulation or reconstructed
 918 points). The simulated RK4 track consists of line segments with known endpoints,
 919 therefore we can calculate the distance of a point from this segment analogically
 920 to Equation 4.25 with \mathbf{v} given as a unit vector in the direction of the segment.

921 We need to find the segment with the lowest distance. We assume, that
 922 the distance $d_{\mathbf{P}}(\tau)$ of a point \mathbf{P} to the point on the track $\mathbf{X}(\tau)$ has a single
 923 minimum (local and global), no local maximum (except the interval endpoints)
 924 and no saddle point

$$\exists! \tau_{\min} \in [0, \tau_N]: (\forall \tau \in [0, \tau_N]: d_{\mathbf{P}}(\tau) \geq d_{\mathbf{P}}(\tau_{\min})) \vee \frac{dd_{\mathbf{P}}}{d\tau}(\tau_{\min}) = 0, \quad (4.28)$$

925 where N is the number of RK4 steps. This is a reasonable assumption for a track
 926 with an approximate shape of a circular arc with a radius r , since the distance d
 927 from a point \mathbf{C} on the corresponding circle of a point \mathbf{P} offset by a from the arc
 928 plane and by b from the arc's center when projected on its plane is given by the
 929 law of cosines:

$$d^2 = a^2 + b^2 + r^2 - 2br \cos \alpha, \quad (4.29)$$

930 where α is the angle between points \mathbf{C} and \mathbf{P} as seen from the center of the arc
 931 (see Figure 4.5). This function is strictly convex for $\alpha \in (-\frac{\pi}{2}, \frac{\pi}{2})$ and in our case,
 932 the center of the arc lies outside of the detector and α is restricted to a small
 933 interval around zero (especially considering that the initial guess should make the
 934 fitted trajectory reasonably close to any relevant point, in the worst-case scenario,
 935 the distance is overestimated which should keep the fit from converging to such
 936 solutions).

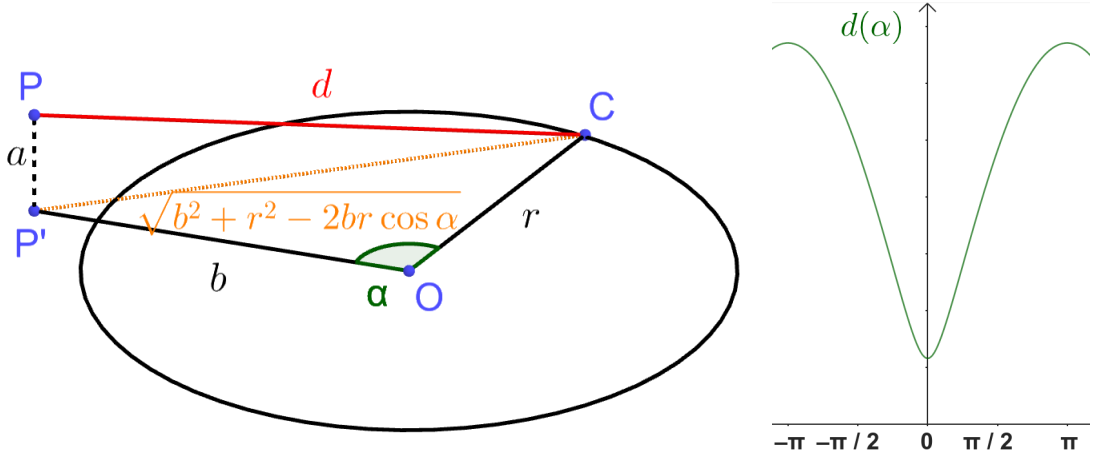


Figure 4.5: Demonstration of the convexity of the distance function $d(\alpha)$ for a circular track (see Equation 4.29).

937 In a more general case, if we consider the vector $\mathbf{a}(\tau) = \mathbf{P} - \mathbf{X}(\tau)$ whose size
938 is $\|\mathbf{a}(\tau)\| = d_{\mathbf{P}}(\tau)$, then we get

$$2d_{\mathbf{P}} \frac{dd_{\mathbf{P}}}{d\tau} = \frac{dd_{\mathbf{P}}^2}{d\tau} = \frac{d}{d\tau} \sum_i a_i^2 = 2 \sum_i a_i \frac{da_i}{d\tau} = 2\mathbf{a} \cdot \frac{d\mathbf{a}}{d\tau} = -2\mathbf{a} \cdot \frac{d\mathbf{X}}{d\tau}, \quad (4.30)$$

939 therefore for the derivative of $d_{\mathbf{P}}(\tau)$ to be zero, $\mathbf{a}(\tau)$ has to be perpendicular
940 to the tangent of the track. In 3D, for a given $\mathbf{X}(\tau)$, this condition restricts \mathbf{P}
941 to a plane. This means that for a curving track we can find a point \mathbf{P} for any
942 two points $\mathbf{X}(\tau), \mathbf{X}(\sigma)$ with non-parallel tangents that has $\frac{dd_{\mathbf{P}}}{d\tau}(\tau) = \frac{dd_{\mathbf{P}}}{d\tau}(\sigma) =$
943 $= 0$, which violates the assumption 4.28. If we have a circle-and-lines track as
944 described in the previous sections, such a point has to lie outside of the circular
945 sector given by the arc.

946 For a planar track, the envelope of all its normals is the evolute of the curve
947 (i.e., the set of centers of all its osculating circles). If the track has a monotonous
948 tangent angle

$$\alpha(\tau) = \text{atan} \frac{\frac{dX_2}{d\tau}}{\frac{dX_1}{d\tau}} \quad (4.31)$$

949 with minimal and maximal α differing by less than π (i.e., the track changes
950 direction by less than 180°), then all intersections of the track's normals must lie
951 on the side of the evolute closer to the track (not obvious?, sometimes the sides
952 are opposite?). At the same time, the intersection must lie in the half planes
953 given by the normals at the beginning and the end of the curve and pointing
954 away from the curve. Together, these three boundaries define a closed shape that
955 will lie outside of the OFTPC for a typical track in our detector.

956 With the assumption 4.28, we can find the segment on the RK4 track with
957 the lowest distance to a given point \mathbf{P} using a binary search algorithm. Let
958 the distance of the point from the n -th vertex be $d_{\mathbf{P},n}$. Then the difference
959 $\Delta d_{\mathbf{P},n} = d_{\mathbf{P},n} - d_{\mathbf{P},n-1}$ satisfies

$$\begin{aligned} \Delta d_{\mathbf{P},n} &< 0 \quad \forall n \text{ such that } \tau_n < \tau_{\min}, \\ \Delta d_{\mathbf{P},n} &> 0 \quad \forall n \text{ such that } \tau_{n-1} > \tau_{\min}. \end{aligned} \quad (4.32)$$

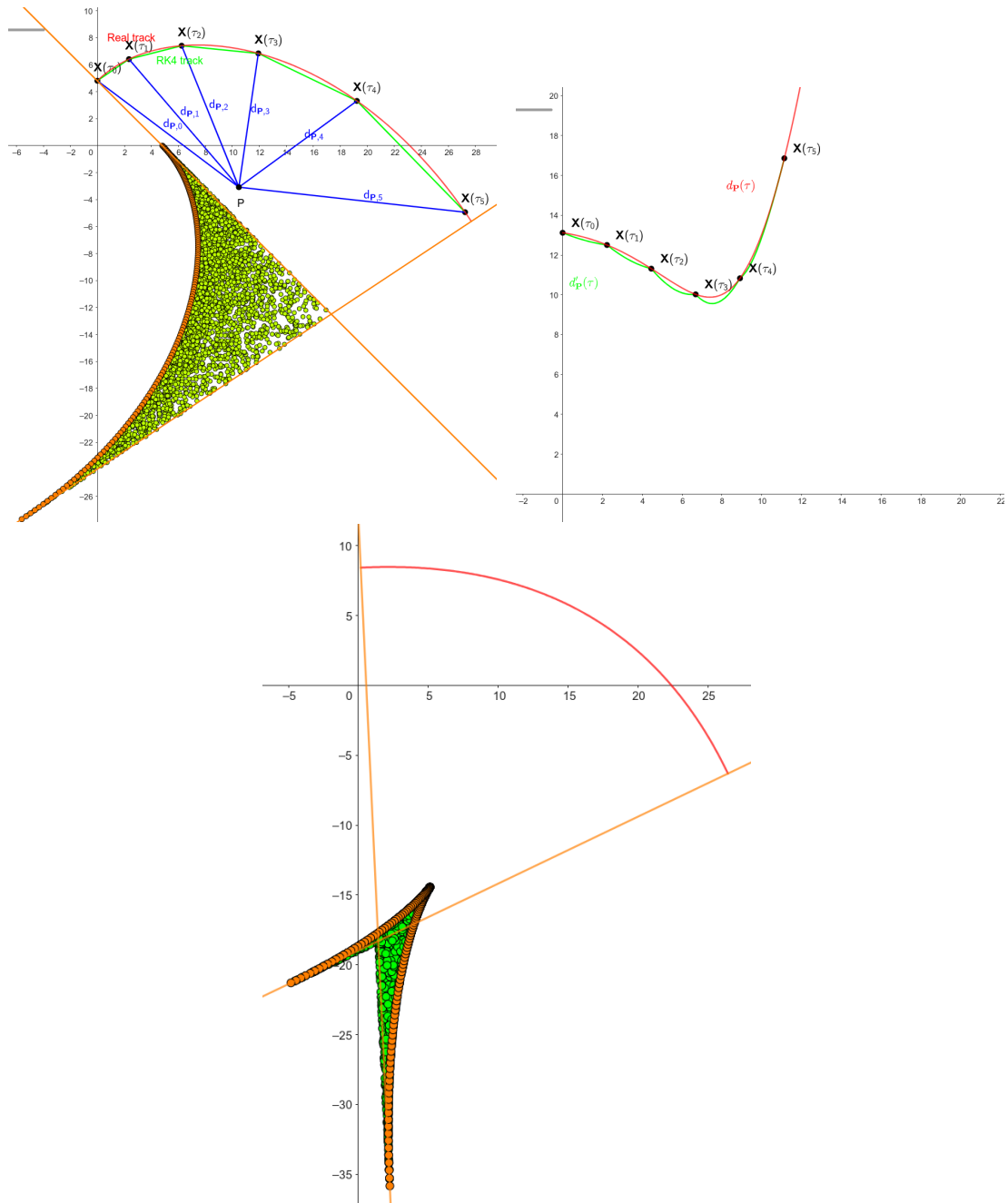


Figure 4.6: some provisional figures

Therefore, we can search for the segment containing $d_{\mathbf{P},\min}$ with binary search starting with $\Delta d_{\mathbf{P},1}$ and $\Delta d_{\mathbf{P},N}$, then calculate the difference $\Delta d_{\mathbf{P},m}$ for the middle index $m = \left\lfloor \frac{N+1}{2} \right\rfloor$. If $\Delta d_{\mathbf{P},m} > 0$ (minor bug in the implementation – if the value for the maximal index is negative, it shouldn't change anything), we can replace the higher index with m , otherwise we replace the lower index. The search stops when the difference between the minimal and maximal index is one. Would it be better if they were the same (maybe not)? Then the minimal value is $d_{\mathbf{P},n-1}$ or $d_{\mathbf{P},N}$ and we can take the minimum of the distances from the two segments connected to $n - 1$. Currently taking the maximal index (and starting at $N - 2$ maximal index $\leftrightarrow N - 1$ -th point), this should be equivalent, since either $\Delta d_{\mathbf{P},\max} > 0$ (in the code is equivalent to max-1 here) or we are at $N - 1$. The minimum of the two distances still taken.

Same details with MIGRAD etc. as previously.

Conclusion

974 Here or at the end of each section. Something about the future of this work?

975 Notes

976 General notes about the thesis:

- 977 • Check that all of the classes and other code are marked the same way in
978 the text. I used italics somewhere, could use different font for this instead.
- 979 • Check unbreakable space in front of articles. Remove excessive article usage
980 with proper nouns.
- 981 • Currently using margins for single-sided printing (bigger on the left side).
- 982 • Check that present tense is used
- 983 • Active vs passive voice usage
- 984 • American English quotation marks (") instead of British English (').
- 985 • Some of the overfull hbox warnings might change if duplex printing is used
986 (they generate black rectangles on the edge of the page), leaving them be
987 for now
- 988 • Check nobreakdash usage (is it always necessary)
- 989 • Check capitalized references (e.g., Figure, Section, Equation)
- 990 • Check \(...\mathbf{\backslash}\) math mode instead of \\$...\$. (actually unlike \[...\] math mode,
991 there is apparently no real benefit to this clumsy syntax)
- 992 • Use siunitx package to ensure correct formatting, physics package for deriva-
993 tives.
- 994 • Check other stuff that's written in the MFF UK template. Apparently it
995 has since been updated and there are some differences (check for them).
- 996 • Check correct subscripts in equation (italics vs no italics)
- 997 • Consistent bold marking of points/vectors
- 998 • Correct footnotes (capital letters, etc.).
- 999 • Might have to mention GeoGebra as per the non-commercial license agree-
1000 ment (Made with GeoGebra®) – maybe put it into acknowledgments next
1001 to the MetaCentrum credit? And list all of the figures where GeoGebra was
1002 used?
- 1003 • Maybe make some section outside of References specifically for literature?
1004 (such as the old CERN TPC review, ATOMKI review is currently not
1005 mentioned, not sure if some Wikipedia articles should get a mention or how
1006 do these things work)
- 1007 • Consistent use of bm vs mathbf

- Consistent use of $\bar{\mathcal{M}}$ instead of \mathcal{M} when talking about the map of the means (so most of the time)
 - Proper equation numbering when deriving a relation
- Random notes:
- Terminology consistency – ionization/primary/secondary electrons
 - Consistent TPC vs OFTPC acronym usage in the text or individual chapters.
 - Only electrons that start and end in the sector closer than 0.5 cm are used for reconstruction (newest version).
 - Attachment, Penning transfer and secondary ionization not considered in the microscopic simulation.
 - Suspicious artifacts of trilinear interpolation in Figure 1.7. **Fixed – integers instead of doubles in the implementation, influenced reconstruction SIGNIFICANTLY (but not simulation).**
 - Profiling of the reconstruction!!!! Find out what's taking the most time (probably Runge-Kutta integration which the fit calls a lot). Could gradually decrease the step size to refine the fit instead of making it small right away (arbitrarily small – the effect of this was never tested). This could take some time to do properly (find a profiler or make profiling macros).
 - Slow drift velocity good for z reconstruction, too low leads to recombination
 - Could add link to the GitHub repository

Future

Things planned for the future:

- Testing the reconstruction algorithm by measuring real particles with a known energy distribution.
- The **Fast Simulation with Ionization Electron Map** is planned for the future. It will use the HEED program [29] to simulate the primary particle and the Ionization Electron Map (see Section 3.2) to simulate the drift of secondary electrons. It should be significantly faster than the Microscopic Simulation but offer comparable precision since it will rely on an already simulated drift map. (Primary track simulated in HEED. Readout parameters by interpolating the map. Diffusion from the map for randomization.)
- Account for GEM, delta electrons, ...
- Likelihood approach instead of least squares (if it improves the reconstruction significantly), we should at least use a better method than taking the center of the TPC bin.
- More detailed electric field simulation (if needed, GEM will have more complex field, some irregularities in the field should be considered)

- 1046 • Account for the triggering in MWPC/TPX3 (particle travels from TPX3
 1047 to MWPC basically immediately – fraction of a nanosecond so there should
 1048 be no significant difference)

1049 **Likelihood - inverse map**

1050 If we wanted to further improve this procedure, taking into account the whole
 1051 map \mathcal{M} , we could make an "inverse map" from \mathcal{R} to distributions on \mathcal{D} . We could
 1052 achieve this by taking the normalized probability density of an electron with initial
 1053 coordinates (x, y, z) having readout coordinates (x', y', t) . If we fix (x', y', t) , we
 1054 get an unnormalized probability density $f(x, y, z) = \mathcal{M}_{(x,y,z)}(x', y', t)$ (assuming
 1055 that all initial coordinates are a priori equally likely). This could potentially
 1056 improve the discrete reconstruction if we take the mean value of this probability
 1057 density across the pad and time bin

$$f_{\text{pad, bin}}(x, y, z) = \frac{1}{A_{\text{pad}} \Delta t_{\text{bin}}} \int_{\text{pad, bin}} \mathcal{M}_{(x,y,z)}(x', y', t) dx' dy' dt \quad (4.33)$$

1058 and using it for a likelihood fit instead of using least squares. This still assumes
 1059 that all initial coordinates are equally likely which is clearly not the case for
 1060 a primary particle track. In the future, we could even use the fast track simulation
 1061 with the map (should be possible to make around 1000 tracks per minute per core
 1062 with current settings), create a big set of tracks with reasonable parameters and
 1063 use these to get an approximation of the probability distribution of the detector
 1064 response. Some approximations would be necessary when interpreting the data to
 1065 decrease the degrees of freedom of this distribution (we would have to pick a set of
 1066 parameters and assume that some of them are independent). This could give us
 1067 an idea about the best achievable resolution (how significantly will the detector
 1068 response differ for a given change in energy). If the difference is significant, we
 1069 could try to further improve the likelihood fit.

Bibliography

- [1] Garfield++. <https://garfieldpp.web.cern.ch/garfieldpp/>. Accessed: 2023-05-18.
- [2] Rene Brun and Fons Rademakers. Root — An Object Oriented Data Analysis Framework. *Nuclear Instruments and Methods in Physics Research Section A: Accelerators, Spectrometers, Detectors and Associated Equipment*, 389(1–2):81–86, Apr 1997. Proceedings AIHENP’96 Workshop, Lausanne, Sep. 1996, See also <https://root.cern/>, Paper published in the Linux Journal, Issue 51, July 1998.
- [3] About MetaCentrum. <https://metavo.metacentrum.cz/en/about/index.html>, 2023. Accessed: 2024-11-27.
- [4] M. E. Rose. Internal Pair Formation. *Phys. Rev.*, 76:678–681, Sep 1949.
- [5] R. Essig, J. A. Jaros, W. Wester, P. Hansson Adrian, S. Andreas, T. Averett, O. Baker, B. Batell, M. Battaglieri, J. Beacham, T. Beranek, J. D. Bjorken, F. Bossi, J. R. Boyce, G. D. Cates, A. Celentano, A. S. Chou, R. Cowan, F. Curciarello, H. Davoudiasl, P. deNiverville, R. De Vita, A. Denig, R. Dharmapalan, B. Dongwi, B. Döbrich, B. Echenard, D. Espriu, S. Fegan, P. Fisher, G. B. Franklin, A. Gasparian, Y. Gershtein, M. Graham, P. W. Graham, A. Haas, A. Hatzikoutelis, M. Holtrop, I. Irastorza, E. Izaguirre, J. Jaeckel, Y. Kahn, N. Kalantarians, M. Kohl, G. Krnjaic, V. Kubarovský, H-S. Lee, A. Lindner, A. Lobanov, W. J. Marciano, D. J. E. Marsh, T. Maruyama, D. McKeen, H. Merkel, K. Moffeit, P. Monaghan, G. Mueller, T. K. Nelson, G. R. Neil, M. Oriunno, Z. Pavlovic, S. K. Phillips, M. J. Pivovaroff, R. Poltis, M. Pospelov, S. Rajendran, J. Redondo, A. Ringwald, A. Ritz, J. Ruz, K. Saenboonruang, P. Schuster, M. Shinn, T. R. Slatyer, J. H. Steffen, S. Stepanyan, D. B. Tanner, J. Thaler, M. E. Tobar, N. Toro, A. Upadye, R. Van de Water, B. Vlahovic, J. K. Vogel, D. Walker, A. Weltman, B. Wojtsekhowski, S. Zhang, and K. Zioutas. Dark Sectors and New, Light, Weakly-Coupled Particles, 2013.
- [6] F.W.N. de Boer, O. Fröhlich, K.E. Stiebing, K. Bethge, H. Bokemeyer, A. Balandia, A. Buda, R. van Dantzig, Th.W. Elze, H. Folger, J. van Klinken, K.A. Müller, K. Stelzer, P. Thee, and M. Waldschmidt. A deviation in internal pair conversion. *Physics Letters B*, 388(2):235–240, 1996.
- [7] F W N de Boer, R van Dantzig, J van Klinken, K Bethge, H Bokemeyer, A Buda, K A Müller, and K E Stiebing. Excess in nuclear pairs near 9 MeV/ invariant mass. *Journal of Physics G: Nuclear and Particle Physics*, 23(11):L85, nov 1997.
- [8] F W N de Boer, K Bethge, H Bokemeyer, R van Dantzig, J van Klinken, V Mironov, K A Müller, and K E Stiebing. Further search for a neutral boson with a mass around 9 MeV/c². *Journal of Physics G: Nuclear and Particle Physics*, 27(4):L29, apr 2001.

- 1111 [9] Attila Vitéz, A. Krasznahorkay, J. Gulyas, Margit Csatlos, Lorant Csige,
 1112 Zoltan Gacsi, Barna Nyakó, F. Boer, T. Ketel, and J. Klinken. Anomalous
 1113 Internal Pair Creation in ${}^8\text{Be}$ as a Signature of the Decay of a New Particle.
 1114 *Acta Physica Polonica B - ACTA PHYS POL B*, 39:483, 02 2008.
- 1115 [10] A. Krasznahorkay, J. Gulyas, Margit Csatlos, Attila Vitéz, T. Tornyi,
 1116 L. Stuhl, Lorant Csige, Zoltan Gacsi, A. J. Krasznahorkay, M. Hunyadi,
 1117 and T.J. Ketel. Searching for a light neutral axial-vector boson in isoscalar
 1118 nuclear transitions. *Frascati Physics Series*, 56:86, 10 2012.
- 1119 [11] A. J. Krasznahorkay, M. Csatlós, L. Csige, Z. Gácsi, J. Gulyás, M. Hunyadi,
 1120 I. Kuti, B. M. Nyakó, L. Stuhl, J. Timár, T. G. Tornyi, Zs. Vajta, T. J. Ketel,
 1121 and A. Krasznahorkay. Observation of Anomalous Internal Pair Creation
 1122 in ${}^8\text{Be}$: A Possible Indication of a Light, Neutral Boson. *Physical Review
Letters*, 116(4), January 2016.
- 1124 [12] D.R. Tilley, J.H. Kelley, J.L. Godwin, D.J. Millener, J.E. Purcell, C.G. Sheu,
 1125 and H.R. Weller. Energy levels of light nuclei A=8,9,10. *Nuclear Physics A*,
 1126 745(3):155–362, 2004.
- 1127 [13] N. J. Sas, A. J. Krasznahorkay, M. Csatlós, J. Gulyás, B. Kertész, A. Krasznahorkay,
 1128 J. Molnár, I. Rajta, J. Timár, I. Vajda, and M. N. Harakeh. Observation of the X17 anomaly in the ${}^7\text{Li}(p,e^+e^-){}^8\text{Be}$ direct proton-capture
 1129 reaction, 2022.
- 1131 [14] A. J. Krasznahorkay, M. Csatlós, L. Csige, J. Gulyás, A. Krasznahorkay,
 1132 B. M. Nyakó, I. Rajta, J. Timár, I. Vajda, and N. J. Sas. New anomaly
 1133 observed in ${}^4\text{He}$ supports the existence of the hypothetical X17 particle.
 1134 *Physical Review C*, 104(4), October 2021.
- 1135 [15] D.R. Tilley, H.R. Weller, and G.M. Hale. Energy levels of light nuclei A =
 1136 4. *Nuclear Physics A*, 541(1):1–104, 1992.
- 1137 [16] A. J. Krasznahorkay, A. Krasznahorkay, M. Begala, M. Csatlós, L. Csige,
 1138 J. Gulyás, A. Krakó, J. Timár, I. Rajta, I. Vajda, and N. J. Sas. New
 1139 anomaly observed in ${}^{12}\text{C}$ supports the existence and the vector character of
 1140 the hypothetical X17 boson. *Phys. Rev. C*, 106:L061601, Dec 2022.
- 1141 [17] F. Ajzenberg-Selove. Energy levels of light nuclei A = 11,12. *Nuclear Physics
A*, 506(1):1–158, 1990.
- 1143 [18] Péter Kálmán and Tamás Keszthelyi. Anomalous internal pair creation. *The
European Physical Journal A*, 56, 08 2020.
- 1145 [19] A. Aleksejevs, S. Barkanova, Yu. G. Kolomensky, and B. Sheff. A Standard
 1146 Model Explanation for the "ATOMKI Anomaly", 2021.
- 1147 [20] Jonathan L. Feng, Bartosz Fornal, Iftah Galon, Susan Gardner, Jordan
 1148 Smolinsky, Tim M. P. Tait, and Philip Tanedo. Protophobic Fifth-Force
 1149 Interpretation of the Observed Anomaly in ${}^8\text{Be}$ Nuclear Transitions. *Phys.
Rev. Lett.*, 117:071803, Aug 2016.

- 1151 [21] Tran The Anh, Tran Dinh Trong, Attila J. Krasznahorkay, Attila Krasznahorkay,
 1152 József Molnár, Zoltán Pintye, Nguyen Ai Viet, Nguyen The Nghia,
 1153 Do Thi Khanh Linh, Bui Thi Hoa, Le Xuan Chung, and Nguyen Tuan Anh.
 1154 Checking the 8Be Anomaly with a Two-Arm Electron Positron Pair Spec-
 1155 trometer. *Universe*, 10(4):168, April 2024.
- 1156 [22] Kh. U. Abraamyan, Ch. Austin, M. I. Baznat, K. K. Gudima, M. A. Kozhin,
 1157 S. G. Reznikov, and A. S. Sorin. Observation of structures at ~ 17 and ~ 38
 1158 MeV/c 2 in the $\gamma\gamma$ invariant mass spectra in pC, dC, and dCu collisions at
 1159 p_{lab} of a few GeV/c per nucleon, 2023.
- 1160 [23] The MEG II collaboration, K. Afanaciev, A. M. Baldini, S. Ban, H. Ben-
 1161 mansour, G. Boca, P. W. Cattaneo, G. Cavoto, F. Cei, M. Chiappini,
 1162 A. Corvaglia, G. Dal Maso, A. De Bari, M. De Gerone, L. Ferrari
 1163 Barusso, M. Francesconi, L. Galli, G. Gallucci, F. Gatti, L. Gerritzen,
 1164 F. Grancagnolo, E. G. Grandoni, M. Grassi, D. N. Grigoriev, M. Hilde-
 1165 brandt, F. Ignatov, F. Ikeda, T. Iwamoto, S. Karpov, P. R. Kettle, N. Kho-
 1166 mutov, A. Kolesnikov, N. Kravchuk, V. Krylov, N. Kuchinskiy, F. Leonetti,
 1167 W. Li, V. Malyshev, A. Matsushita, M. Meucci, S. Mihara, W. Mol-
 1168 zon, T. Mori, D. Nicolò, H. Nishiguchi, A. Ochi, W. Ootani, A. Oya,
 1169 D. Palo, M. Panareo, A. Papa, V. Pettinacci, A. Popov, F. Renga, S. Ritt,
 1170 M. Rossella, A. Rozhdestvensky, S. Scarpellini, P. Schwendimann, G. Sig-
 1171 norelli, M. Takahashi, Y. Uchiyama, A. Venturini, B. Vitali, C. Voena,
 1172 K. Yamamoto, R. Yokota, and T. Yonemoto. Search for the X17 particle
 1173 in ${}^7\text{Li}(\text{p}, \text{e}^+\text{e}^-){}^8\text{Be}$ processes with the MEG II detector, 2024.
- 1174 [24] Adam Abed Abud, Bima Abi, R. Acciarri, M. Acero, M. Adames,
 1175 G. Adamov, Mark Adamowski, Dianna Adams, M. Adinolfi, Christopher
 1176 Adriano, A. Aduszkiewicz, Juan Antonio Aguilar Sánchez, Z. Ahmad,
 1177 Jawaira Ahmed, B. Aimard, Fijay Akbar, B. Ali-Mohammadzadeh, T. Alion,
 1178 K. Allison, and R. Zwaska. A Gaseous Argon-Based Near Detector to En-
 1179 hance the Physics Capabilities of DUNE. 03 2022.
- 1180 [25] Stewart C. Loken, H. Aihara, M. Alston-Garnjost, D. H. Badtke, J. A.
 1181 Bakken, A. Barbaro-Galtieri, A. V. Barnes, B. A. Barnett, B. Blumenfeld,
 1182 A. Bross, C. D. Buchanan, W. C. Carithers, O. Chamberlain, J. Chiba, C.
 1183 Y. Chien, A. R. Clark, O. I. Dahl, C. T. Day, P. Delpierre, K. A. Derby,
 1184 P. H. Eberhard, D. L. Fancher, H. Fujii, T. Fujii, B. Gabioud, J. W. Gary,
 1185 W. Gorn, N. J. Hadley, J. M. Hauptman, B. Heck, H. Hilke, J. E. Huth,
 1186 J. Hylen, H. Iwasaki, T. Kamae, R. W. Kenney, L. T. Kerth, R. Koda, R. R.
 1187 Kofler, K. K. Kwong, J. G. Layter, C. S. Lindsey, S. C. Loken, X-Q. Lu,
 1188 G. R. Lynch, L. Madansky, R. J. Madaras, R. Majka, J. Mallet, P. S. Mar-
 1189 tin, K. Maruyama, J. N. Marx, J. A. J. Matthews, S. O. Melnikoff, W. Moses,
 1190 P. Nemethy, D. R. Nygren, P. J. Oddone, D. Park, A. Pevsner, M. Pripstein,
 1191 P. R. Robrish, M. T. Ronan, R. R. Ross, F. R. Rouse, G. Shapiro, M. D.
 1192 Shapiro, B. C. Shen, W. E. Slater, M. L. Stevenson, D. H. Stork, H. K. Ticho,
 1193 N. Toge, M. Urban, G. J. Van Dalen, R. van Tyen, H. Videau, M. Wayne,
 1194 W. A. Wenzel, R. F. vanDaalen Wetters, M. Yamauchi, M. E. Zeller, and
 1195 W-M. Zhang. Performance of the signal processing system for the time

- 1196 projection chamber. *IEEE Transactions on Nuclear Science*, 30(1):162–166,
1197 1983.
- 1198 [26] Misbah Uddin Ahmed. Simulation of the electron and ion movement through
1199 a 4-GEM stack, 2021. Institut für Kernphysik.
- 1200 [27] Marmelad. 3D interpolation2.svg, 2025. Licensed under CC BY-SA 3.0
1201 (<https://creativecommons.org/licenses/by-sa/3.0/legalcode>). Accessed: 9-April-2025.
- 1203 [28] Cmglee. Trilinear interpolation visualisation, 2025. Licensed under
1204 CC BY-SA 3.0 (<https://creativecommons.org/licenses/by-sa/3.0/legalcode>). Accessed: 26-March-2025.
- 1206 [29] I.B. Smirnov. Modeling of ionization produced by fast charged particles in
1207 gases. *Nuclear Instruments and Methods in Physics Research Section A: Ac-
1208 celerators, Spectrometers, Detectors and Associated Equipment*, 554(1):474–
1209 493, 2005.
- 1210 **Acknowledgments:** Computational resources were provided by the e-INFRA
1211 CZ project (ID:90254), supported by the Ministry of Education, Youth and Sports
1212 of the Czech Republic.

1213 List of Figures

1214 0.1	The ATOMKI anomalous IPC measured for different nuclei.	5
1215 0.2	Results from the Hanoi spectrometer – angular e^+e^- pair correlations measured in the ${}^7\text{Li}(p, e^+e^-){}^8\text{Be}$ reaction at $E_p = 1225$ keV [21].	6
1216 0.3	Results from the MEG II experiments – angular correlation of e^+e^- pairs with $E_{\text{sum}} \in [16, 20]$ MeV measured in the ${}^7\text{Li}(p, e^+e^-){}^8\text{Be}$ reaction with proton beam energies 500 and 1080 keV. The 500 keV dataset is fitted with Monte Carlo of both the IPC deexcitation and the EPC produced by gammas [23].	7
1217 0.4	Schematics of the detector at the Van der Graaff facility at IEAP CTU.	7
1218 1219 1220 1221 1222		
1223 1.1	Particle identification in the PEP-4 TPC at SLAC based on the energy loss per distance $\frac{dE}{dx}$ [24].	10
1224 1.2	Schematic view of the PEP-4 TPC [25]. A charged particle produced in a collision in the beam pipe creates a spiral ionization track in the magnetic field. The central cathode then accelerates ionization electrons towards the endcap anode wires where they are multiplied and read out.	10
1225 1.3	A scanning electron microscope image of a GEM foil.	13
1226 1.4	Garfield simulation of an avalanche in a GEM hole [26]. An incoming electron (orange) is accelerated in the strong electric field of the GEM and causes further ionization multiplying the number of free electrons (orange). Most of the produced cations (red) are captured by the GEM cathode.	13
1227 1.5	Schematics of the first sector OFTPC with detector space coordinates.	16
1228 1.7	Magnetic field simulation results. The OFTPC volume and the vacuum tube are marked with black lines, the magnets are marked with red lines. The coordinates of the magnets from the CAD drawing seem to be 9/10 of the ones from the magnetic simulation (confirm and fix).	17
1229 1.6	Pad layout of the OFTPC and its parameters. Pads 102, 124 and 127 are irregular, the rest has the same dimensions.	17
1230 1.8	Visualization of trilinear interpolation as a composition of linear interpolations (inspired by [27]). We want to interpolate the value in the red point C. First we interpolate between the four pairs of blue points sharing the last two indices along the x -axis (Eq. 1.14), then between the two pairs of the resulting green points along the y -axis (Eq. 1.15) and finally between the two resulting orange points along the z -axis to get the final red value (Eq. 1.16).	18
1231 1.9	Geometric interpretation of trilinear interpolation as expressed in Equation 1.18. The colored dots represent the values in given points and the colored boxes represent the volume in the opposite corner by which the corresponding values are multiplied. The black dot represents the interpolated value which is multiplied by the entire volume [28].	19
1232 1233 1234 1235 1236 1237 1238 1239 1240 1241 1242 1243 1244 1245 1246 1247 1248 1249 1250 1251 1252 1253 1254 1255 1256 1257		

1258	2.1	Example of a simulated electron track in 70 % argon and 30 % CO ₂ atmosphere (on the left). Swap for better images, better zoom. Explain drift lines, primary particle.	21
1259			
1260			
1261	2.2	Comparison of diffusion in a simulated electron track in 70 % argon, 30 % CO ₂ atmosphere and in 90 % argon, 10 % CO ₂ atmosphere (on the right). Swap for better image, better zoom. Or put the same pictures for both comparisons in one subfigure, etc. Describe better.	21
1262			
1263			
1264			
1265			
1266	3.1	Dependence of the drift time on the z coordinate in 90 % argon and 10 % CO ₂ atmosphere, fitted with a linear function. The fitted function gives us the average drift velocity in the gas and can be used for rough reconstruction in our TPC. Swap for better image with axis labels, etc. Maybe write the fitted equation.	25
1267			
1268			
1269			
1270			
1271	3.2	The first attempt of a track reconstruction using only the drift velocity. This approach works well in a standard TPC (ideally cite some source). 90 % argon and 10 % CO ₂ atmosphere. Swap for better image, correct coordinates.	26
1272			
1273			
1274			
1275	3.3	First attempt at a track reconstruction using only the drift velocity, residues. Swap for better image, correct coordinates. What's causing the shift? Explain details.	26
1276			
1277			
1278	3.4	Example of map generation. Swap for better image, correct coordinates.	29
1279			
1280	3.5	Example reconstruction with the map. Swap for better image, correct coordinates.	29
1281			
1282	3.6	Selection of the points for interpolation. Create better images; use the explanation interpolation vs. extrapolation strange property. Solution 2 probably does not make much sense.	32
1283			
1284			
1285	4.1	Example of a fitted reconstructed track. Swap for better image.	34
1286	4.2	First attempt at a track reconstruction using only the drift velocity. Spline energy reconstruction attempt. Swap for better image(s) – subfigure environment, correct coordinates.	36
1287			
1288			
1289	4.3	First attempt at a track reconstruction using only the drift velocity. Circle and Lines Fit in 2D. Swap for better image, correct coordinates. Bias should be described in the previous chapter, not here.	38
1290			
1291			
1292			
1293	4.4	Circle and Lines Fit 3D geometry. Swap for better image.	41
1294	4.5	Demonstration of the convexity of the distance function $d(\alpha)$ for a circular track (see Equation 4.29).	42
1295			
1296	4.6	some provisional figures	43

₁₂₉₇ **List of Tables**

1298 List of Abbreviations

- 1299 **GEM** Gas Electron Multiplier
- 1300 **HEED** High Energy Electro-Dynamics
- 1301 **IEAP CTU** Institute of Experimental and Applied Physics, Czech Technical
1302 University in Prague
- 1303 **IPC** Internal Pair Creation
- 1304 **EPC** External Pair Creation
- 1305 **Micromegas** MICRO-MEsh GAseous Structure
- 1306 **MWPC** Multi-Wire Proportional Chamber
- 1307 **OFTPC** Orthogonal Fields TPC
- 1308 **RK4** Runge-Kutta 4th order
- 1309 **TPC** Time Projection Chamber
- 1310 **ToA** time-of-arrival
- 1311 **ToT** time-over-threshold
- 1312 **TPX3** Timepix 3